SEARCH FOR THE FLAVOR-CHANGING NEUTRAL CURRENT IN TOP PAIR EVENTS WITH AN ASSOCIATED PHOTON USING 13 TEV PROTON-PROTON COLLISION DATA COLLECTED WITH THE ATLAS DETECTOR

by

JASON TYLER BARKELOO

A DISSERTATION

Presented to the Department of Physics
and the Graduate School of the University of Oregon
in partial fulfillment of the requirements
for the degree of
Doctor of Philosophy

March 2020

DISSERTATION APPROVAL PAGE

Student: Jason Tyler Barkeloo

Title: Search for the Flavor-Changing Neutral Current in Top Pair Events With an Associated Photon Using 13 TeV Proton-Proton Collision Data Collected With the ATLAS Detector

This dissertation has been accepted and approved in partial fulfillment of the requirements for the Doctor of Philosophy degree in the Department of Physics by:

David Strom	Chair
James Brau	Advisor
Spencer Chang	Core Member
Dev Sinha	Institutional Representative

and

Janet Woodruff-Borden	Vice Provost and Dean of the Graduate School

Original approval signatures are on file with the University of Oregon Graduate School.

Degree awarded March 2020

DISSERTATION ABSTRACT

Jason Tyler Barkeloo

Doctor of Philosophy

Department of Physics

March 2020

Title: Search for the Flavor-Changing Neutral Current in Top Pair Events With an Associated Photon Using 13 TeV Proton-Proton Collision Data Collected With the ATLAS Detector

Abstract for FCNC here.

This dissertation includes previously published and unpublished co-authored material.

CURRICULUM VITAE

NAME OF AUTHOR: Jason Tyler Barkeloo

GRADUATE AND UNDERGRADUATE SCHOOLS ATTENDED:
University of Oregon, Eugene, Oregon
Miami University, Oxford, Ohio
Wittenberg University, Springfield, Ohio

DEGREES AWARDED:
Doctor of Philosophy, Physics, 2020, University of Oregon
Master of Sceience, Physics, 2012, Miami University
Bachelor of Science, Physics, 2010, Wittenberg Univeristy

PROFESSIONAL EXPERIENCE:

University of Oregon, Graduate Research Assistant, ATLAS Experiment, June 2014-Present

University of Oregon, Graduate Teaching Assistant, September 2012-June 2014

Miami University, Teaching and Research Assistant, August 2010 - May 2012

Wittenberg University, Undergraduate Researcher, August 2008 - May 2010

GRANTS, AWARDS AND HONORS:

Weiser Senior Teaching Assistant Award – University of Oregon – 2014

American Association of Physics Teachers Outstanding Teaching Assistant – Miami University – 2012

PUBLICATIONS:

J. Barkeloo, J. Brau, M. Breidenbach, R. Frey, D. Freytag, C. Gallagher, R. Herbst, M. Oriunno, B. Reese, A. Steinhebel, D. Strom. "A silicon-tungsten electromagnetic calorimeter with integrated electronics for the International Linear Collider" J. Phys.: Conf. Ser. **1162** 012016 (2019).

J. Kangara, A. Hachtel, M. C. Gillette, J. Barkeloo, E. Clements, S. Bali. "Design and construction of cost-effective fail-safe tapered amplifier systems for laser cooling and trapping experiments", Am. J. Phys. **82**(8), 805 - 817 (2014).

A. Hachtel, J. Kleykamp, D. Kane, M. Marshall, B. Worth, J. Barkeloo, J. Kangara, J. Camenisch, M. Gillette, S. Bali. "An undergraduate lab on measurement of radiative broadening in atomic vapor", Am. J. Phys. **81**(6), 471 (2013).

Additional ATLAS Collaboration publications can be found:
http://inspirehep.net/search?p=exactauthor%3AJason.Barkeloo

TABLE OF CONTENTS

LIST OF FIGURES

Figure Page

Figure Page

LIST OF TABLES

Table Page

CHAPTER I

THE LARGE HADRON COLLIDER AND THE ATLAS DETECTOR

This chapter describes the experimental details of the collider complex at the LHC and specifically the ATLAS detector used to produce, collect, and measure various particle properties. The subsystems of the ATLAS detector are described in detail.

1.1. The Large Hadron Collider

The LHC is the world's largest and most energetic particle accelerator. As a hadron collider the LHC collides particles made up of quarks, typically proton-proton collisions. Protons, as opposed to electrons/positrons at a previous collider such as LEP, have much higher mass and a significantly smaller amount of energy loss during acceleration due to synchrotron radiation (which scales as $\frac{1}{m^4}$). Due to this the LHC is able to reach a much higher center of mass energy using the same circular ring used by LEP, though this higher energy comes at a cost. Due to hadrons being made up of constituent partons (quarks and gluons), not all of which interact in any given collision, the particles that do not take place in the hard interaction are left over and create a 'messier' environment in the detectors. This is opposed to lepton colliders, where all of the energy that goes into the collision is present in the final state particles coming from the interaction point. The implication of this is that at hadron colliders the momentum along the beam axis cannot be known, only momentum in the transverse plane of a collision is known due to conservation of momentum.

The LHC is housed in a 27 km ring running beneath the Franco-Swiss border near Geneva, Switzerland and accelerates beams of protons (ions) to a center of mass

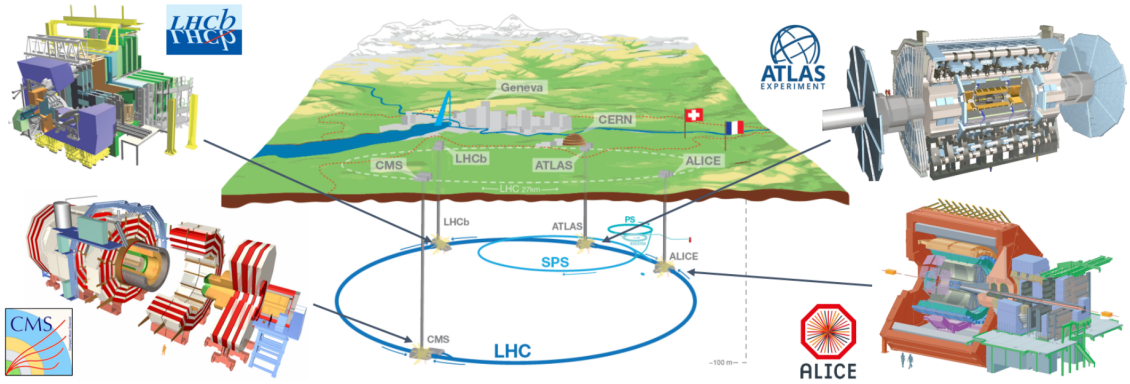

FIGURE 1.1. Map of LHC and the various detector experiments: ATLAS, CMS, LHCb, and ALICE located under the Franco-Swiss border near Geneva[1]

energy of 13 TeV (5 TeV) using two counterpropagating circular beams around the ring. The particles are then collided at one of the four primary interaction points, each of which house a dedicated detector as shown in Figure 1.1.

In addition to the LHC beam line the accelerator uses a series of smaller accelerators to increase the energy of the particles before being introduced into the LHC. This accelerator complex is detailed in Figure 1.2. The start of the accelerator chain, and source of LHC protons, is the Linear Accelerator 2 (LINAC 2, purple) where hydrogen gas is placed inside of an electric field that separates the protons and electrons. The remaining protons are passed through radiofrequency (RF) cavities and accelerated to 50 MeV using electric fields which oscillate at a frequency specific to the distance between any two RF cavities.

After leaving LINAC 2 the protons are injected into the Proton Synchrotron Booster (BOOSTER, light purple) and accelerated to 1.4 GeV before being passed to the Proton Synchrotron (PS, magenta) in two batches with a separation of 1.2 seconds. The PS accelerates the protons to 25 GeV to be injected into the Super Proton Synchrotron (SPS, blue) in a series of four batches separated by 3.6 seconds and are accelerated to 450 GeV. The SPS is the second largest accelerator in the

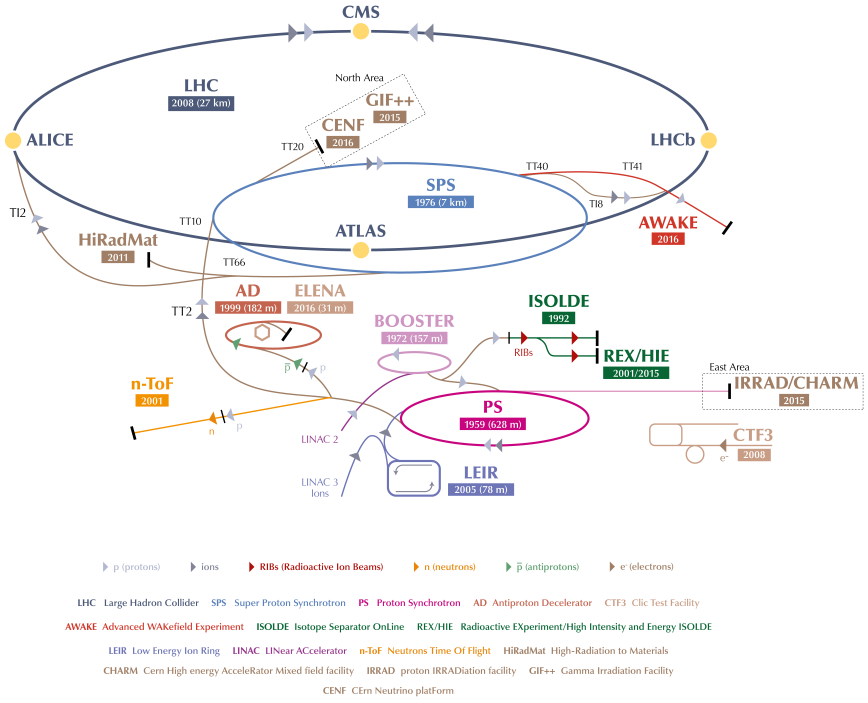

FIGURE 1.2. Schematic of the CERN accelerator complex.[2]

complex. After reaching the 450 GeV of the SPS the particles are split and injected into the LHC in opposing directions where they are further accelerated to a collision energy of 6.5 TeV per beam leading to a center of mass energy of 13 TeV for the LHC during Run-2.

The first proton-proton collisions were produced in the LHC in 2008 at the injection energy of the SPS, $\sqrt{s} = 900$ GeV. During testing a faulty electrical connection caused a magnet quench, or a sudden loss of superconductivity, to occur. This broke the nearby magnets and caused a delay in operations until late 2009 when LHC Run-1 began at a collision energy of $\sqrt{s} = 7$ TeV and later raised to $\sqrt{s} = 8$ TeV in 2012 to complete Run-1. Various upgrade and repairs on the LHC occurred

throughout the long shutdown between 2012-2015 where the center of mass energy was increased to the LHC Run-2 energy of $\sqrt{s} = 13$ TeV.

1.1.1. LHC Magnets

The energies achieved in the collisions are only possible due to the LHC magnets that bend and focus the colliding particles. The LHC uses the most powerful magnet technology that can be produced on an industrial scale. There are 1232 superconducting dipole magnets each being 15m in length, weighing over 35 tons, and producing uniform magnetic fields of up to 8.4 T. The niobium-titanium cables must be cooled to 1.9 K and operate with a current of 11,800 A. Of these 1232 magnets 1104 are used to bend the particles around the ring and the remaining 128 are used in the beam dump. To achieve the same center of mass energy using standard non-superconducting magnets the 27 km LHC would instead have to be upwards of 120 km long.

Since the bunches of particles are charged they will naturally diverge while traveling if not focused. To correct for this an additional 392 quadrupole magnets, 5-7m in length, are used to focus the beam. These quadrupoles are used in pairs: one which focuses in the horizontal plane and defocuses in the vertical plane and the other which focuses in the vertical plane and defocuses in the horizontal plane. Together these magnets keep the beam squeezed to a usable size. All of these magnets have two aperatures, one for each of the counter-propagating beams.

1.1.2. Luminosity

The amount of data collected at collider experiments is determined not only by the center of mass energy of colliding particles but also the rate of events produced.

This rate is called the luminosity and can be determined by the square of the number of particles in each bunch (since any one in one bunch can interact with any one in the other), the time between bunches, and the cross section of the bunch (or probability of a collision).

$$\mathcal{L} = \frac{1}{\sigma}\frac{dN}{dt}$$

For any given proton-proton pair the luminosity can be expressed as:

$$\mathcal{L} = \frac{1}{4\pi\sigma_x\sigma_y}$$

and can be expanded for the whole beam with the inclusion of the number of protons per bunch (N_1 and N_2), the number of bunches (N_b), and the frequency at which the bunches overlap (f) to:

$$\mathcal{L} = \frac{N_1 N_2 N_b f}{4\pi\sigma_x\sigma_y}$$

which can be iterated over the running time of the LHC (the total time with beams of proper size and energy propagating through the LHC) giving the total delivered luminosity. This total integrated luminosity as a function of time during LHC Run-2 is shown in Figure 1.3. This luminosity value can be mulitplied by the probability, or cross section, of any particular final state to obtain the number of times that final state is produced with a given luminosity.

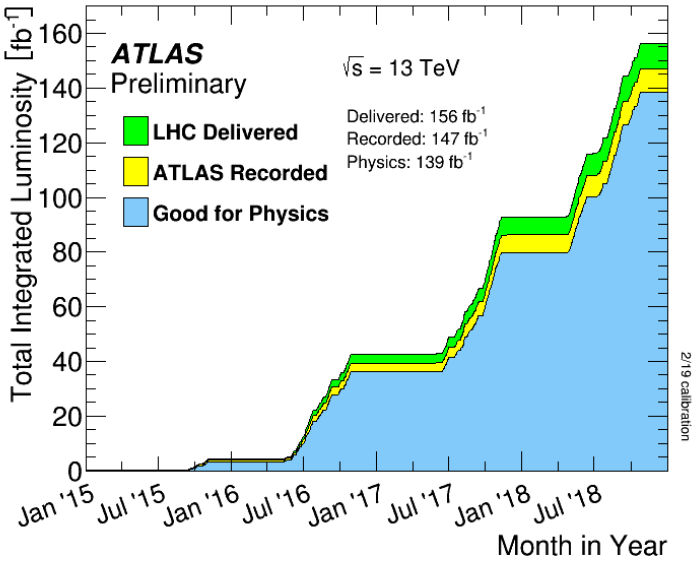

FIGURE 1.3. Total integrated luminosity as a function of time delivered by the LHC(green), recorded (yellow) and declared good for physics analysis (blue) by the ATLAS detector throughout Run 2 consisting entirely of 13 TeV pp collisions. [3]

1.1.3. Pileup

Increasing the luminosity is very beneficial for increasing the statistics needed when searching for rare events but it brings additional challenges as well. Most interactions at any given detector are not hard-scatter events that correspond to poentially interesting physics cases but are instead soft collisions which create noise in the various detector experiments. The LHC works hard to deliver as much data to the experiments as possible and delivers bunches of protons at a time. It is possible for multiple pairs of protons to undergo these soft inelastic collisions at a time. The average number of interactions per bunch crossing, or pileup $\langle\mu\rangle$, for Run-2 was 33.7, shown in Figure 1.4. The pileup must be accounted for when separating the tracks and energy deposited from an interesting hard-scatter event from the other soft collisions which occur at nearly the same time within a detector. The difficulty of separating out one event from another can be seen in Figure 1.5 where there are 28 reconstructed

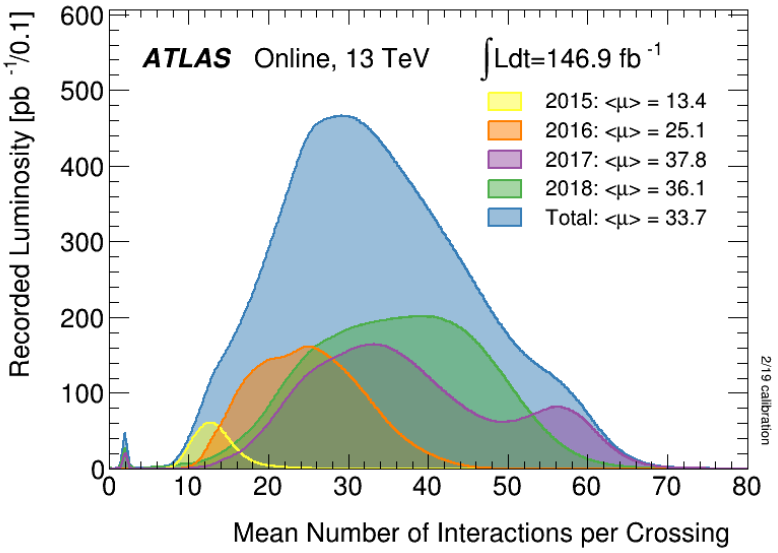

FIGURE 1.4. Luminosity-weighted distribution of the mean number of interactions per bunch crossing for the entirety of Run 2 shown by individual years, 2015 (yellow), 2016(orange), 2017 (purple), 2018 (green), as well as an integrated total (blue).[3]

verticies. An extreme case of 65 reconstructed verticies is also shown in Figure 1.6. As the LHC will continue to operate at higher and higher luminosities in the future, the amount of pileup that will need to be dealt with will continue to increase.

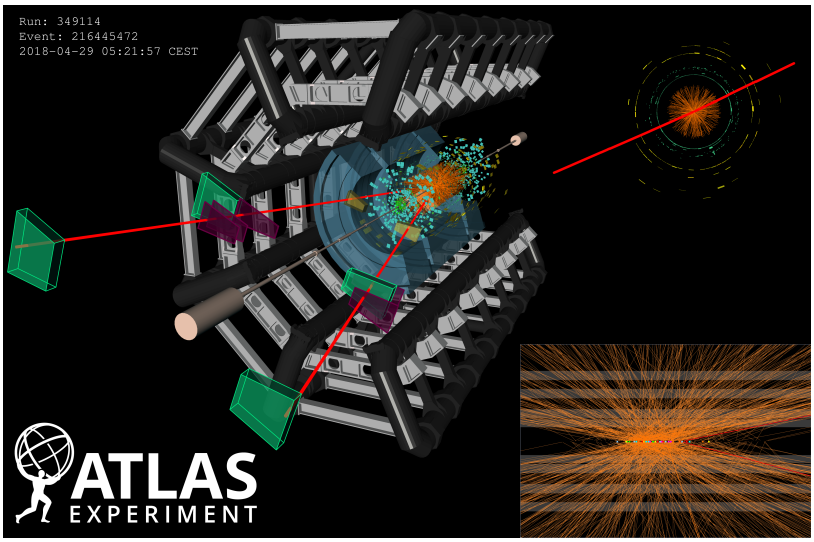

FIGURE 1.5. A candidate dimuon event ($Z \rightarrow \mu^+\mu^-$) with 28 reconstructed verticies collected in 2018 with the ATLAS detector.[3]

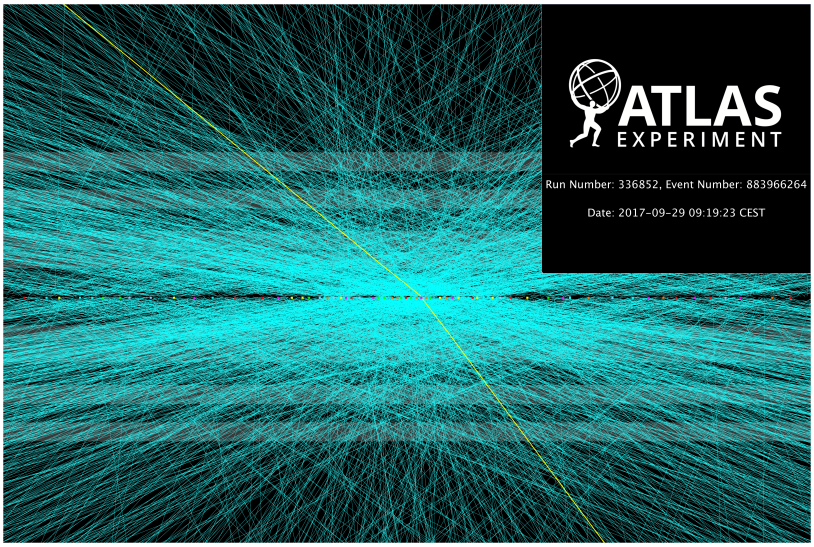

FIGURE 1.6. A candidate dimuon event ($Z \rightarrow \mu^+\mu^-$) with 65 reconstructed verticies collected in 2017 with the ATLAS detector.[3]

1.2. The ATLAS Detector

The ATLAS dectector, depicted in Figure 1.7, is one of the two general-purpose detectors at the LHC. It is the largest detector of its kind ever built at 46 meters in length, 25 meters in diameter, weighing 7000 tons, and containing around 3000 kilometers of cables[4]. Around the interaction points within the detector the ATLAS detector covers nearly the entire solid angle and is nominally symmetric. ATLAS is built up of a variety of concentric subsystems, which will be discussed throughout this section, each with a specialized task and optimized for the measurement of different particle signatures. The primary subsystems used to measure particle trajectories and momenta accurately are the inner detector (Section 1.2.3), the hadronic and electromagnetic calorimeters (Section 1.2.4), and the muon system (Section 1.2.5). The inner detector measures the paths of charged particles, called tracks. The electromagnetic and hadronic calorimeters measure the energy of charged and neutral

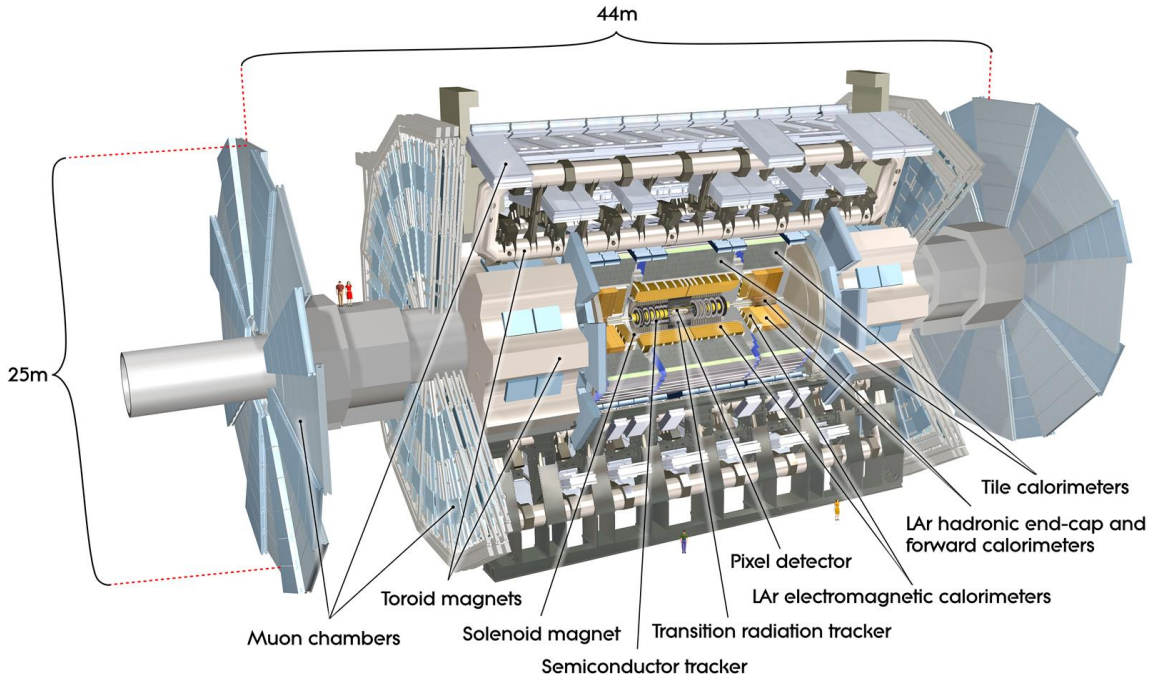

FIGURE 1.7. Schematic of the ATLAS detector.[4]

particles. The muon system measures the momenta of minimum ionizing particles (MIPs).

In addition to the various detectors and calorimeters the ATLAS detector has a magnet system (Section 1.2.2) that bends charged particles in the detector, allowing for a measurement of their charge and momentum and distingushing them from neutral particles. Between the inner detector and the calorimeters is a solenoid which provides an axial magnetic field. Between the calorimeters and the muon system is a toroidal magnet, from which ATLAS got its original acronym (**A** **T**oroidal **L**HC **A**pparatu**S**).

1.2.1. Common Detector Variables and the ATLAS Coordinate System

The ATLAS detector uses a right-handed coordinate system with the origin at the interaction point. In a Cartesian coordinate system the z-axis is defined to be along the beam pipe (positive towards LHC Point 8) while the x-axis points toward the center of the LHC ring which means the positive y-axis points upwards as shown in Figure 1.8. In practice coordinates used are a modified polar coordinate system. In the transverse (xy-)plane to the beam line the azimuthal angle, ϕ, is measured around the beam axis and radius, r, are used. Away from the transverse plane the pseudorapidity, η, is defined by the polar angle (from the y-axis), θ, to be $\eta = -\ln[\tan(\theta/2)]$. Differences in η are Lorentz invariant under longitudinal boosts such that the differences in the rest frames of colliding particles are not important for massless particles. Since the particles typically present in the ATLAS detector are highly energetic, and therefore have a large boost, the pseudorapidity is a good estimate of the true rapidity of the particles. Massless particles are also produced uniformly in η and not in θ which is why η is preferred.

The distance between any two objects within the ATLAS detector can be described geometrically by the variable $\Delta R = \sqrt{\Delta\eta^2 + \Delta\phi^2}$. Another common variable used is the missing transverse energy, E_T^{miss}. The information known about the missing energy is limited to the transverse plane because the momenta of the colliding particles is unknown along the beamline.

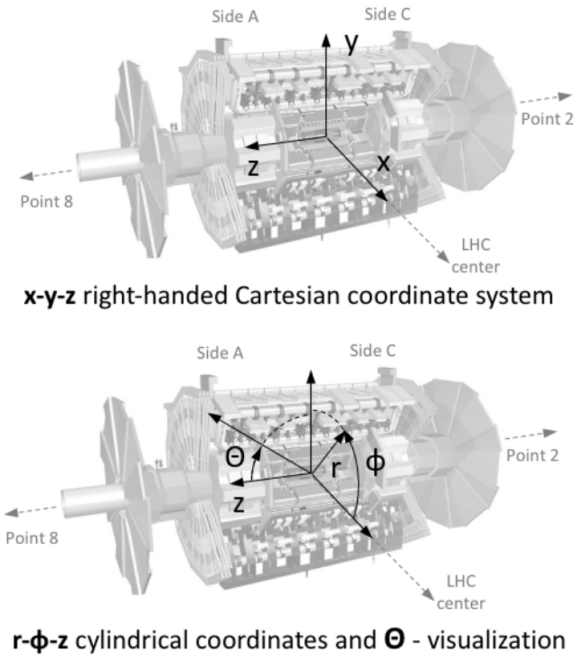

FIGURE 1.8. Coordinate system used in the ATLAS Collaboration.[1]

1.2.2. Magnet Setup

The ATLAS detector has two magnet systems of note. The first is the superconducting solenoid that surrounds the inner detector with a magnetic field aligned with the beam axis. The solenoid has a magnetic field of 2T that makes the tracking of charged particles possible with the inner detector. This magnet is a thin single layer coil, which is imperative to minimize the amount of material in front of the calorimeters.

The toroid system consist of two parts, the end-cap and the barrel magnets. The windings of these magnets is shown in Figure 1.9. Each of these magnets consists of eight superconducting air-core coils, together weighing 830 tons. The end-cap coils are interleaved with the barrel coils. A peak magnetic field strength of 3.9T (4.1T) is acheived in the barrel (end-cap) toroid which assists in the track and momentum

measurement of high energy muons as they leave the ATLAS detector. The barrel toroids cover a range of $|\eta| < 1.4$ while the endcap toroids cover the range $1.6 < |\eta| < 2.7$. The remaining region is covered by a combination of the field of the two sets of toroids.

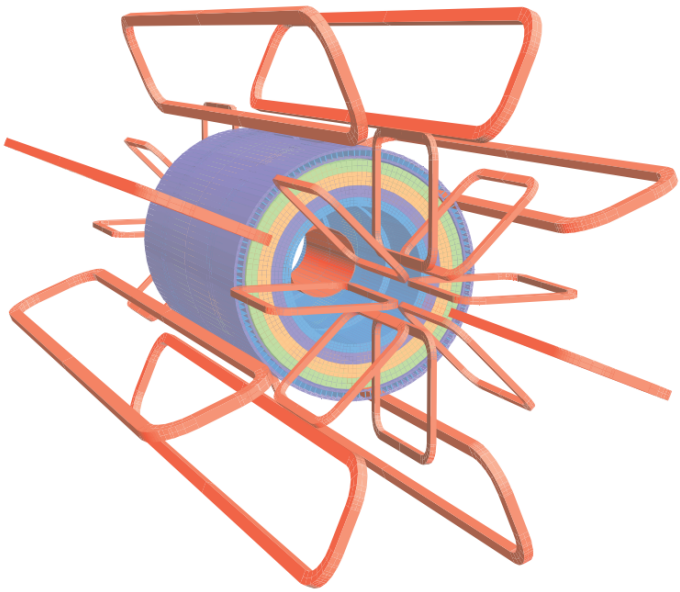

FIGURE 1.9. Schematic of the windings of the ATLAS magnet.[4]

1.2.3. Inner Detector

The inner detector sits inside the solenoid magnet and is used to reconstruct charged particle tracks as they bend due to the magnetic field. The inner detector is made up of four distinct parts. The Insertable B-Layer (IBL) [5], the Pixel Detectors, the Semiconductor Tracker (SCT), and the Transition Radiation Tracker (TRT)[6]. The inner detector provides complete coverage for charged particle tracking, extending to $|\eta| < 2.5$. Momentum resolution as well as primary and secondary vertex measurements are done using the inner detector. Secondary verticies are important for identifying of particles with delayed decays such as bottom quarks (Section 2.3.4.1),

charm quarks, and tau leptons. A schematic of the inner detector can be seen in Figure 1.12.

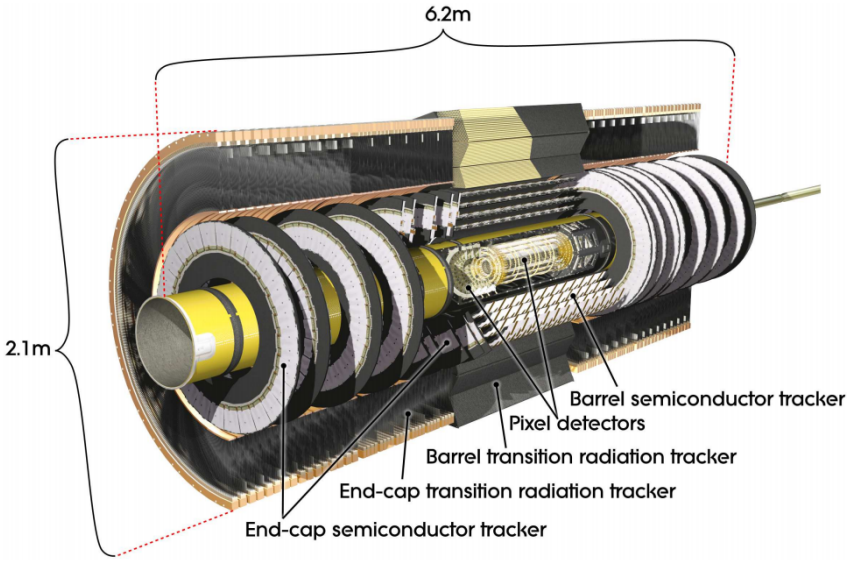

FIGURE 1.10. Schematic of the ATLAS inner detector.[4]

The IBL was added during Long Shutdown I (2016) of the LHC and is closer to the interaction point than the innermost layer in Run 1. This required adding a smaller beam pipe (reduction in radius from 29 mm to 25mm) but was able to improve the resolution of verticies and thus the reconstruction of events involving bottom quark decays as well as allowing for charm quark decays to be classified better than ever before. This improvement is shown in Figure 1.11 in a study of the impact parameter resolution. An improvement of up to 40% is seen with the inclusion of the IBL in the low p_T region. The IBL functions as a fourth layer of the Pixel Detector and uses planar sensors (similar to the Pixel Detector) as well as 3D sensors allowing electrons to interact with the bulk of the sensor as opposed to just the surface.

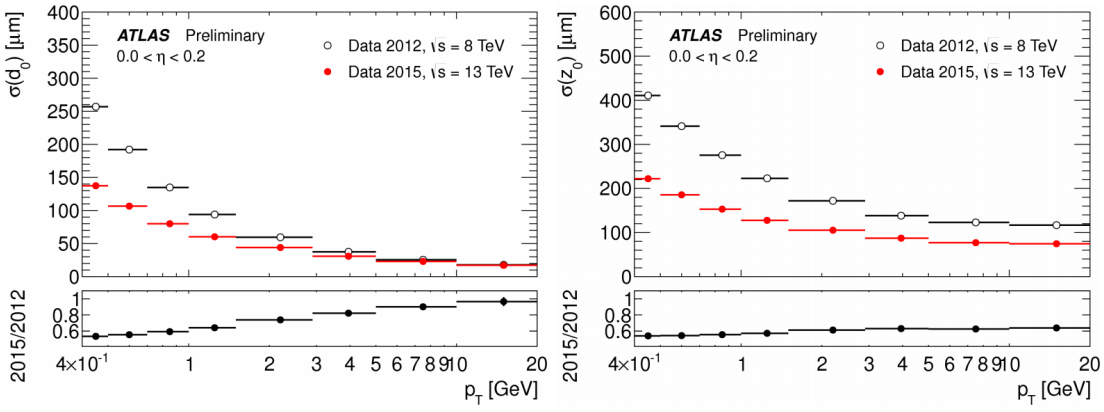

FIGURE 1.11. Unfolded transverse (left) and longitudinal (right) impact parameter resolution measured with (Run 2) and without (Run 1) the IBL as a function of p_T.[7]

The next layer from the beam pipe, as detailed in Figure 1.12, is the Pixel Detector which is a series of high granularity silicon pixel detectors which measure a position when a charged particle passes through them. These silicon pixels are n-doped silicon wafers biased with a high voltage that allow for the creation of electron hole pairs. The electron then drifts toward the electrode which creates the position signal in the readout electronics. In addition to the IBL there are three more cylindrical layers which are designed to ensure single pixel isolation and minimize leakage. The pixels are $50 \times 400 \mu\text{m}^2$. For complete coverage to the cylindrical system, endcaps are placed on each side of the central barrel. These endcaps consist of four wheels that have trapezoid shaped silicon pixels. The three barrel layers consist of 67 million pixels and the endcaps total an additional 13 million pixels. After the Pixel Detector is the Semiconductor Tracker (SCT) which is also made up of barrel and endcap detecors. The barrel SCT is four cylindrical layers of silicon microstrip trackers where the endcaps are nine discs on each side of the barrel made up of either silicon or galium arsenide semiconductors. The SCT contains over 60m^2 of silicon detectors with over 6 million readout channels.

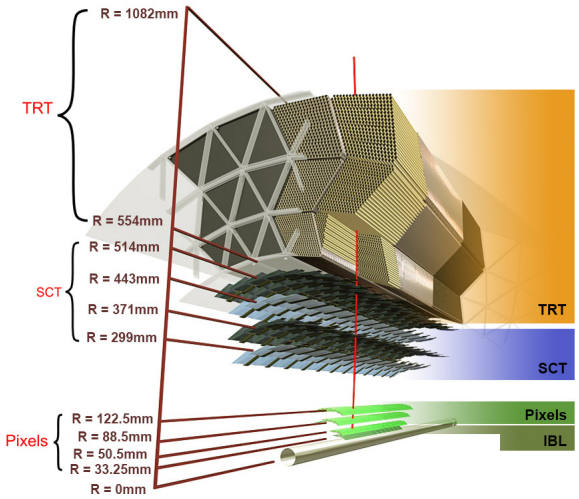

FIGURE 1.12. Blown up schematic of the ATLAS inner detector with more detail.[8]

The final part of the Inner Detector is the Transition Radiation Tracker (TRT) [9]. The TRT is a straw detector surrounding the SCT. Every straw is a 4 mm in diameter Kapton tube with a 0.03 mm diameter gold-plated tungsten wire in its center. In the barrel region there are 50,000 straws that are each 144 cm long and an additional 250,000 straws in both endcaps which are 39 cm in length. Each straw is filled with an active gas mixture made up of mostly Xenon or Argon.

When charged particles traverse across the TRT straws they ionize the active gas mixture and produce ionization clusters. The amount of clusters created depends on how far the charged partcile traveled through the TRT (5-6 clusters per mm). The straw walls are held at a high negative voltage such that the primary electrons are accelerated toward the gold-plated tungsten wire anode creating more ionization by liberating more electrons from the active gas and producing a detectable signal which is amplified and read out. Transition radiation occurs when a particle makes a transition between materials with different dielectric constants and the energy radiated is directly proportional to the Lorentz factor of the particle. This allows for an excellent discrimination between electrons and charged pions.

1.2.4. Electromagnetic and Hadronic Calorimeters

While the inner detector focuses on tracking the charged particles as they pass through the detector the ATLAS Calorimeter system is designed to absorb and measure the energy of neutral and charged particles. The exceptions to this are muons which are able to penetrate through the calorimeters into the muon and neutrinos which do not interact at all within the ATLAS detector. The calorimeters can be broken down into two major systems, the Liquid Argon (LAr) calorimeter[10] and the tile calorimeter (TileCal)[11]. Both of these systems are shown in Figure 1.13.

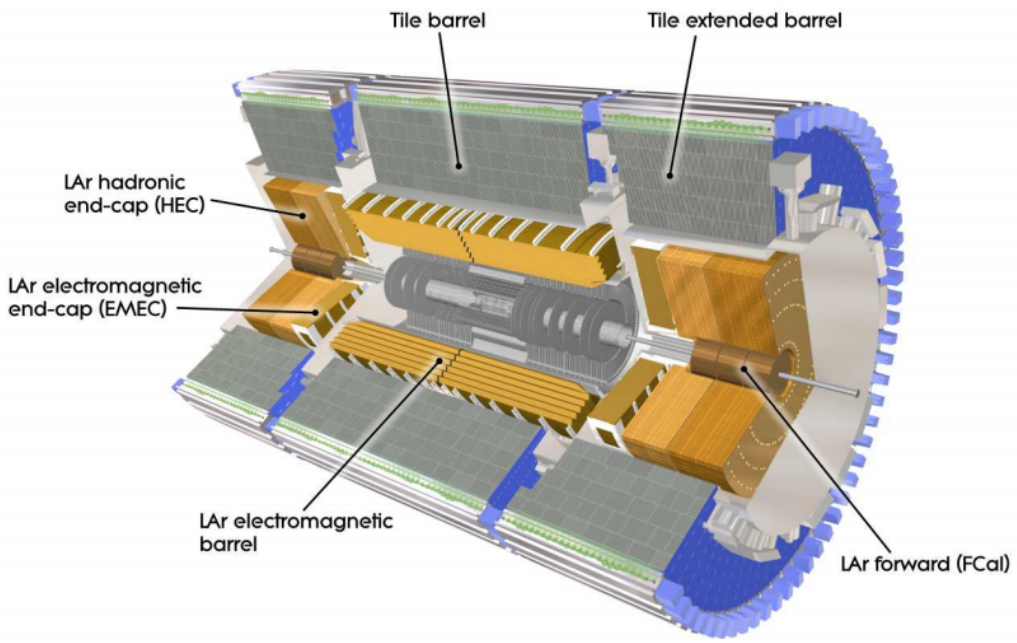

FIGURE 1.13. Schematic of the ATLAS hadronic and electromagnetic calorimeter systems.[4]

The LAr calorimeter is a sampling calorimeter. Sampling calorimeters use alternating layers of a dense absorbing material and an active material to measure the signal produced by showering particles. The LAr calorimeter uses lead as the absorbing material and liquid argon measured with copper-tungsten sensors as the

active layer. The layers in the LAr calorimeter are arranged in an "accordian-shaped" geometry shown in Figure 1.14 to provide complete azimuthal coverage. This allows for the electromagnetic energy resolution to be uniform in the azimuthal direction. Sampling calorimeters do not directly measure the entire energy of the particle, only the interactions that occur in the active layers. The stochastic nature of the processes being measured means that large fluctuations can occur while measuring electromagnetic showers. These flucuations mean that sampling calorimeters must account for sampling statistics as opposed to other types of calorimeters where the entirety of the energy is absorbed with an active layer, such as scintillators.

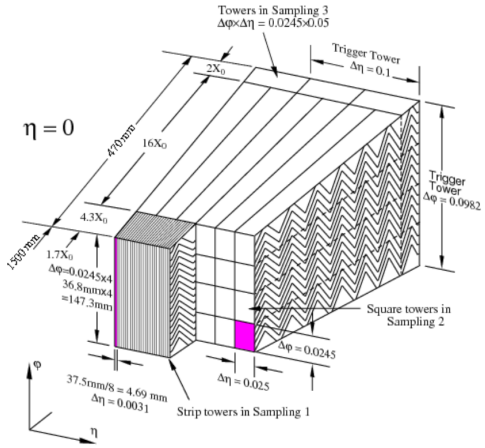

FIGURE 1.14. Sketch of the accordian structure used in the LAr Calorimeter.[10]

For sampling calorimeters it is important to know the ratio $\frac{E_{\text{visible}}}{E_{\text{deposited}}}$ so that the energy of a particle can be reconstructed based on only the energy measured by the active layers. This ratio must be measured with test beams where the original beam energy is known precisely. Sampling calorimeters allow for the complete detection of electromagnetic showers. Because there is a large amount of material to traverse through, all of the energy can be deposited within the detector. The amount of material travesed by each particle is an important aspect as it includes not only the

active material and absorber but also the support structures and cables that can play a role in particle interactions. The thickness of a material passed through is typically measured in radiation lengths (X_0), where an electron passing through one radiation length will lose 1/e of its energy to bremsstrahlung. The amount of radiation lengths in the LAr calorimeter is shown in Fugre 1.15.

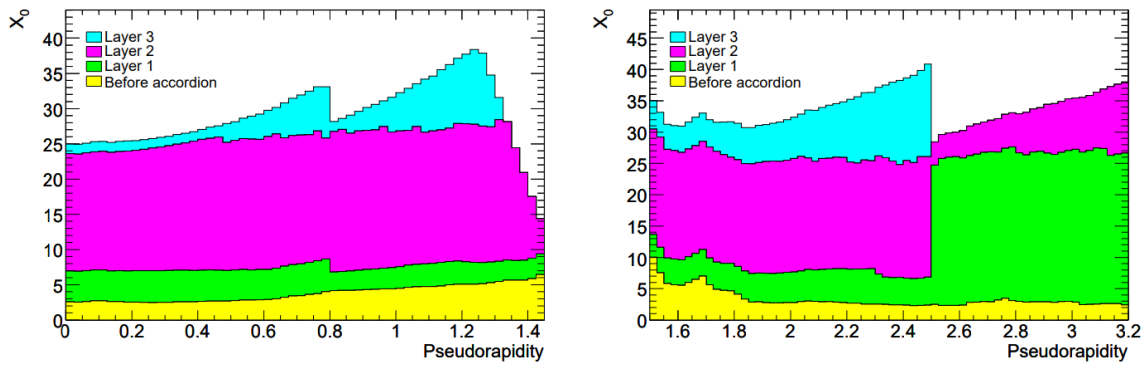

FIGURE 1.15. Number of radiation lengths throughout the LAr calorimeter as a function of $|\eta|$[4]

Forward from the barrel there are two electromagnetic endcap (EMEC) wheels with a similar accordion structure to the modules in the barrel that cover ranges $1.4 < |\eta| < 2.5$ and $2.5 < |\eta| < 3.2$. Outside of the EMEC wheels is the LAr hadronic endcap (HEC) with a simpler parallel plate structure. The last part of the LAr calorimeter is the LAr forward calorimeter (FCal). Due to the FCal's proximity to the beamline the particle flux is very high so a dense calorimeter is used to avoid losing energy into other pieces of the detector. The FCal is made up of three layers: the first is copper and the others are tungten.

The remaining calorimeter system is the TileCal which is primarily responsible for hadronic calorimetry in the central region $|\eta| < 1.7$. TileCal is also a sampling calorimeter with iron plate absorbers and plastic scintillating tiles. The scintillating tiles are placed orthogonal to the beamline and readout using wavelength shifting

fibers connected to photomultiplier tubes on the outside of the system. TileCal has a fixed central barrel and two extended barrel sections as shown in Figure 1.13. The extended barrel sections can be moved. The total nuclear interaction length of the TileCal is 7.4λ, where λ is the mean distance a hadronic particle will travel before experiencing an inelastic interaction with the material it is traveling through. The total interaction length for each section of the calorimeter is shown in Figure 1.16.

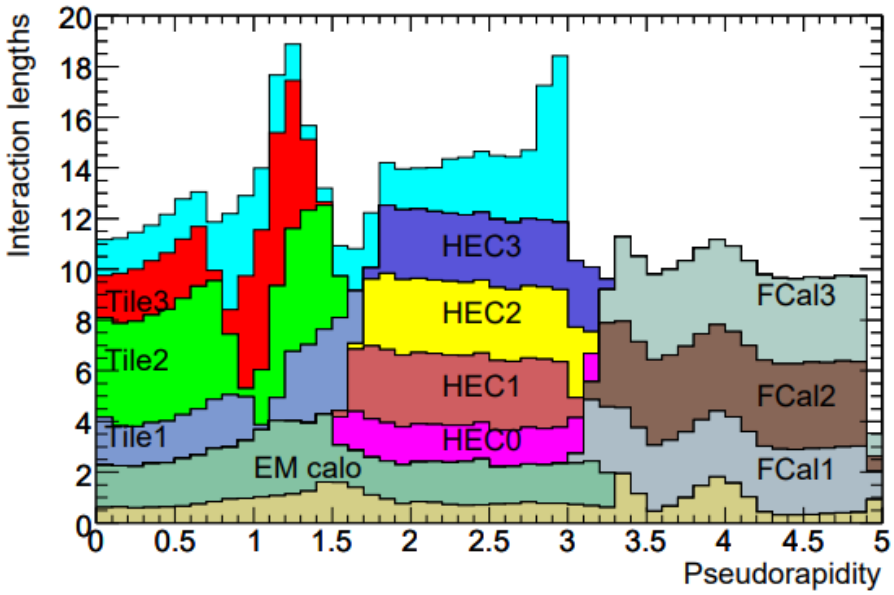

FIGURE 1.16. Number of interaction lengths throughout the LAr calorimeter as a function of $|\eta|$

1.2.5. Muon System

The final and outermost subdetector of the ATLAS detector is the muon spectrometer, which measures the momentum of muons. Different technologies are used in the barrel and endcap regions for both measurement and triggering (deciding which events to keep when only a small fraction of events can be recorded). For the barrel region, $|\eta| < 2.7$, three layers of Monitored Drift Tubes (MDT) are used for

precision energy and tracking measurements and Resistive Plate Chambers (RPC) for triggering. In the forward region, $2.0 < |\eta| < 2.7$, where the flux is higher, Cathode Strip Chambers (CSC) are used for energy and position measurements, and Thin Gap Chambers (TGC) are used for triggering. These systems, shown in Figure 1.17, are aided by the magnetic field created by the toroid system discussed in Section 1.2.2.

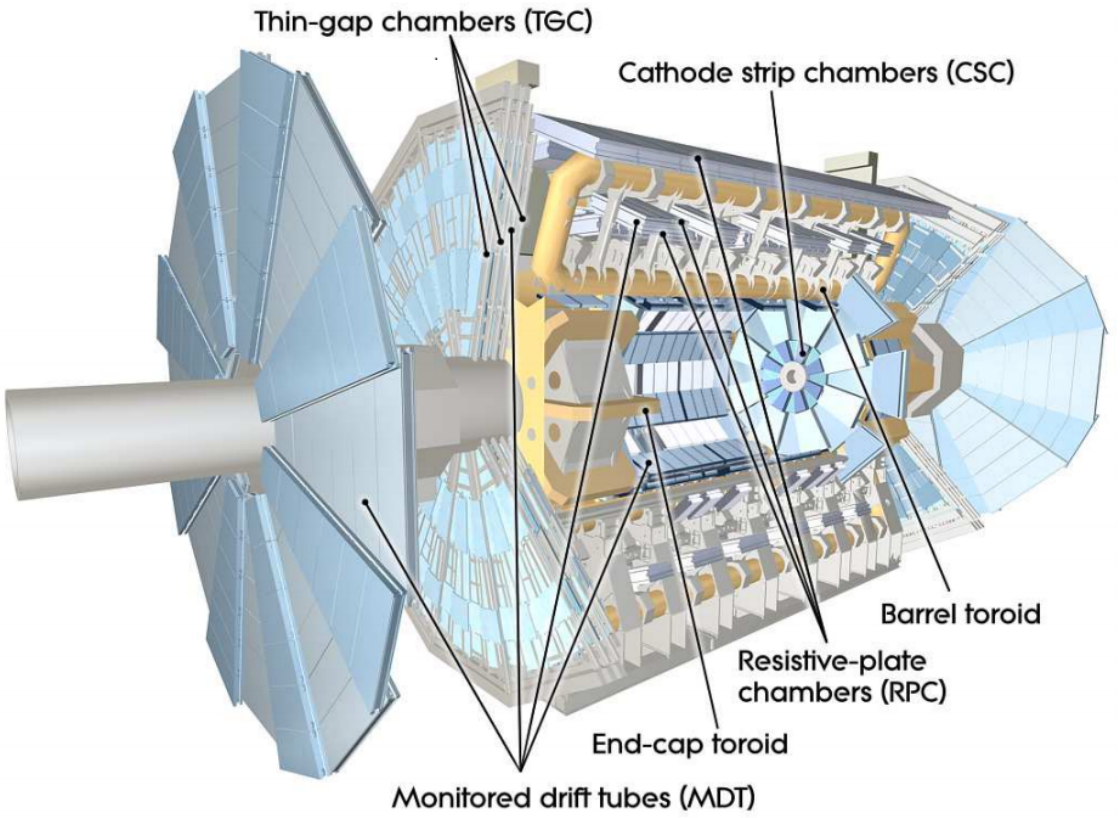

FIGURE 1.17. Schematic of the ATLAS muon detector.[4]

MDTs are arranged in chambers of up to 6 layers of aluminum tubes ranging in length from one to six meters. Each tube is 30 mm in diameter and contains a sense wire 50μm in diameter. The chambers are arranged with a support spacer in between layers of MDTs that have a built-in optical sensor to monitor the drift tubes (hence the name) for deformations. This ensures that the precision of measurements does

not change over time. The MDTs are only used in the barrel and not in the forward region because they are inappropriate in areas with high rates, in this case a high flux of muons.

For the forward region CSCs are used. CSCs consist of arrays of positively charged wires crossed with negatively charged strips within a gas. As muons pass through they knock electrons from atoms in the gas which go toward the anode wires. Since the strips and wires are perpendicular to each other two position coordinates are read out. CSCs have the benefit of giving acceptable one and two-track resolution in a high flux environment.

The trigger system for muons in the barrel region uses RPCs which are parallel plates with opposite charges separated by a gaseous volume. A muon passing through an RPC knocks electrons from the gas which cause an avalanche of electrons that get picked up by the external metal strips rather than by the electrode. The pattern of metal strips that gets hit gives a quick measurement of the muon momentum which is used by the trigger to make the immediate decision about the event. The endcap muon trigger relies on TGCs. TGCs are anode wires with graphite cathodes in between thin layers of fiberglass laminate. Similarly to why CSCs are used over MDRs in the forward region TGCs have excellent timing resolution and can handle the high flux of muons in the forward regions.

1.2.6. Trigger and Data Acquisition

The amount of data the LHC is capable of producing is staggering, and the ATLAS trigger system is required to reduce the enormous amount of data produced to a reasonable amount while keeping the most interesting events. The LHC provides collisions at a rate of 40MHz. Every event saved to tape requires about 1.6MB of

space [12]. To keep all of the data produced 64TB/s would need to be saved or 230PB of data for a 12-hour run or 400EB of data per year (150 days of uptime).

In order to reduce this to a manageable level the ATLAS trigger system uses a two level trigger system. A hardware trigger, Level 1 or L1 trigger, is used to lower the rate from 40MHz to between 75 and 100kHz which is sent to the next level of the trigger system, the High Level Trigger (HLT). Another factor of 50 in rate reduction is achieved by this software based HLT to reduce the rate below 2kHz. A flowchart of the ATLAS trigger and data acquisition system is shown in Figure 1.18. When combined with partial event readouts and the <2kHz full event readout the total bandwidth requirement is around 3GB/s to be written. This means that only around 0.004% of data is stored.

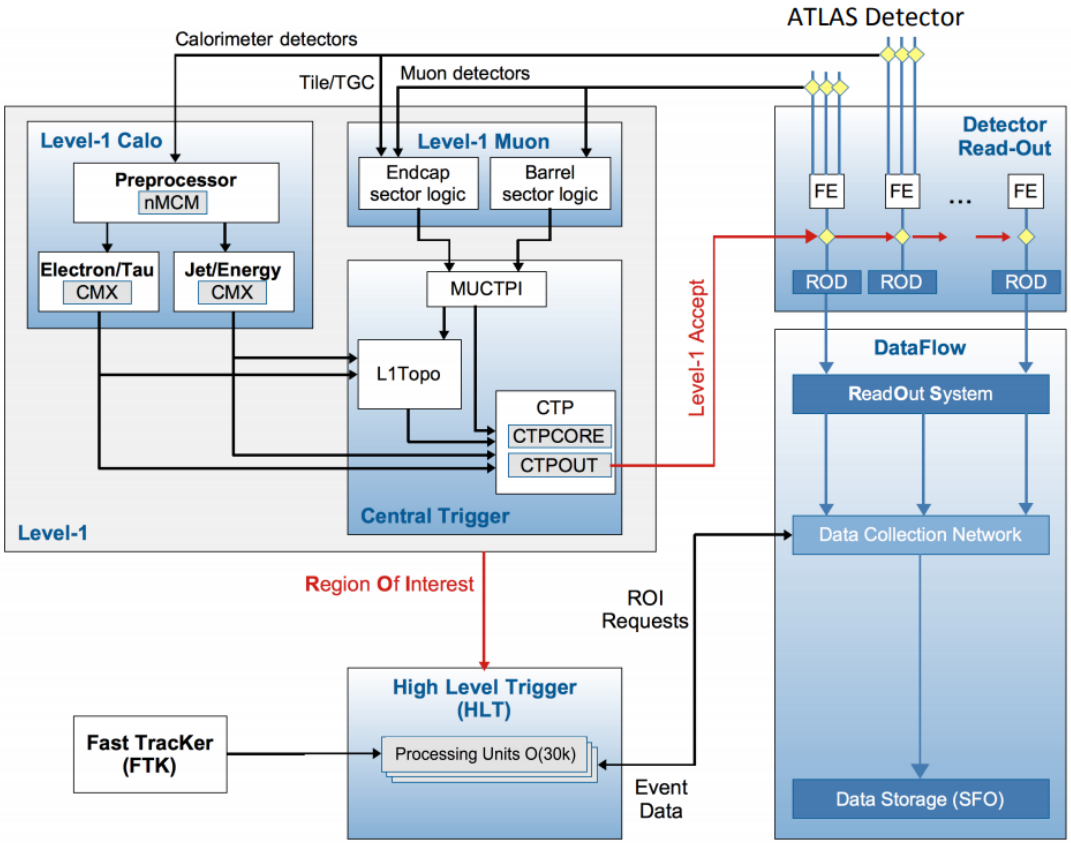

FIGURE 1.18. Flow diagram of the ATLAS trigger and data acquisition system used in Run 2.[13]

1.2.6.1. Level 1 Calorimeter

The Level 1 hardware trigger uses geometrically coarse information from some of the subdetectors. The data from the calorimeters is sent to the Level 1 Calorimeter (L1 Calo) system. L1 Calo uses low granularity information to identify Regions of Interest (RoIs) from objects that interact in the calorimeters (e.g., photons, electrons, jets, taus), events with high total energy, as well as events with an imbalance of energy coming from missing transverse energy. The information is fed into the L1 Calo system and through a preprocessor that allows L1 Calo to handle the effects within ATLAS from pileup events. Data from TileCal and the trigger portions of the muon systems

goes to the Level 1 Muon (L1 Muon) system which applies various logical processes to determine wheter or not an event should be kept. Outputs from L1 Calo and L1 Muon are passed to the Central Trigger Processor (CTP) which provides a level 1 trigger accept and LHC timing information to the detector read out. At the same time the CTP gives RoIs to the HLT.

1.2.6.2. High Level Trigger

The HLT takes RoIs from the CTP as well as full detector granularity and makes a further decision whether that event should be saved. This is done using a computing farm of over 40,000 cores that run over 2,500 independent algorithms (trigger chains) on the RoIs. The HLT can provide partial and full event reconstruction depending on the event stream the event is decided to be within. The main event stream is the physics analysis stream which gets full event reconstruction, while the other streams typically only require partial event reconstruction. The other streams are used for a variety of things such as trigger level analysis, monitoring of the subsystems, and calibrating the detector.

CHAPTER II

SIMULATION AND RECONSTRUCTION

This chapter presents details on the simulation of various physics processes and the reconstruction of physics objects for both simulated events and data events.

2.1. Simulation of pp Collisions

To draw conclusions from ATLAS experimental data it is necessary to make accurate theoretical predictions about the processes being searched for. Having accurate background models can help identify when a data signal is behaving in a way that might suggest new physics. Due to the stochastic nature of particle physics collisions and interactions, it is not practical to create exact predictions. Instead the ATLAS experiment uses Monte Carlo (MC) simulations to model physical behaviors. MC simulations are done by repeated random sampling of possible physical processes that can occur at any given time to a particle. The possibilities change based on factors such as particle energy and particle environment. A flow chart for the entire simulation chain is shown in Figure 2.1.

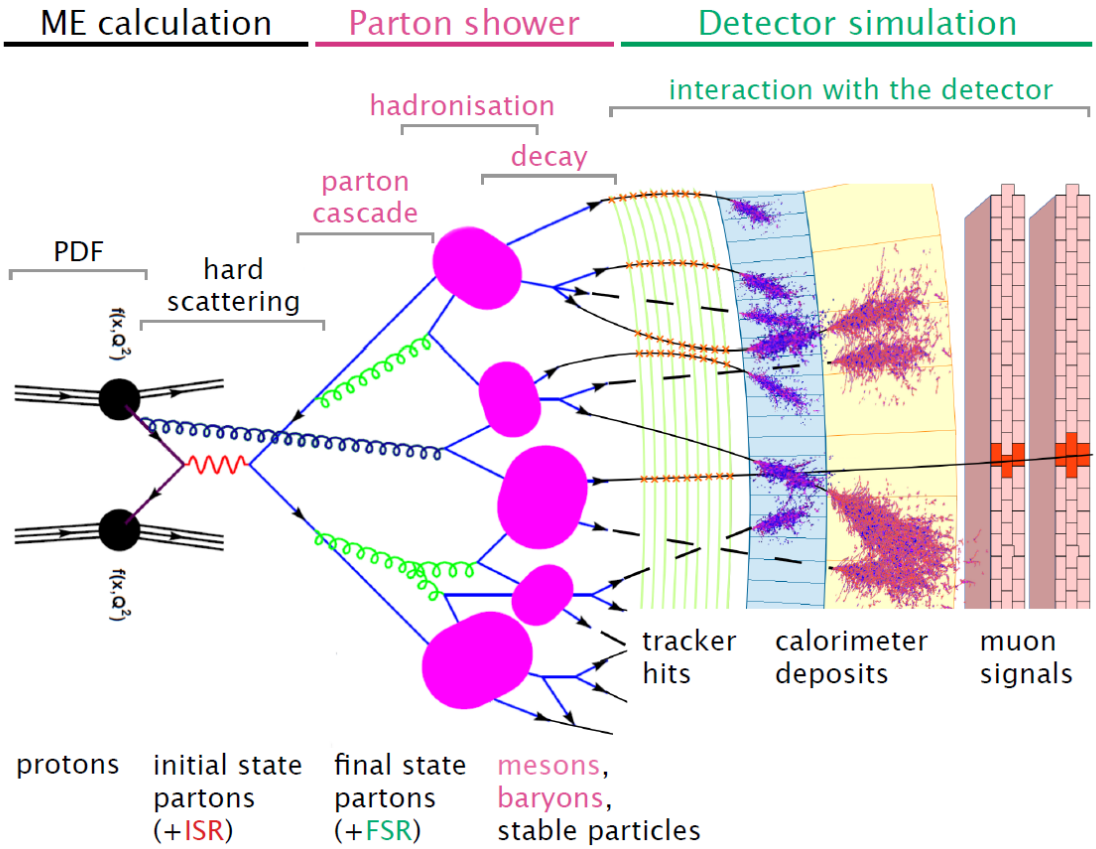

FIGURE 2.1. A pictoral view of the different steps for the creation of a MC event. [14]

2.1.1. Matrix Element Calculation and Parton Distribution Functions

Particle interactions at LHC energies do not involve the entire proton. The constituent partons that create the proton (the two up quarks, down quark, and the sea of gluons) are what interact in any given event. The gluons create many virtual quark-antiquark pairs which can interact as well. The valence quarks, the two up quarks and the down quark that make up the proton, are the major portion of interacting partons at low energies, mainly inelastic interactions. At LHC energies deep inelastic scattering is possible and the sea quarks play a more dominant role. Proton structure is described by a Parton Distribution Function (PDF) which gives

the probability of finding any parton with a particular momentum fraction, is shown in Figure 2.2.

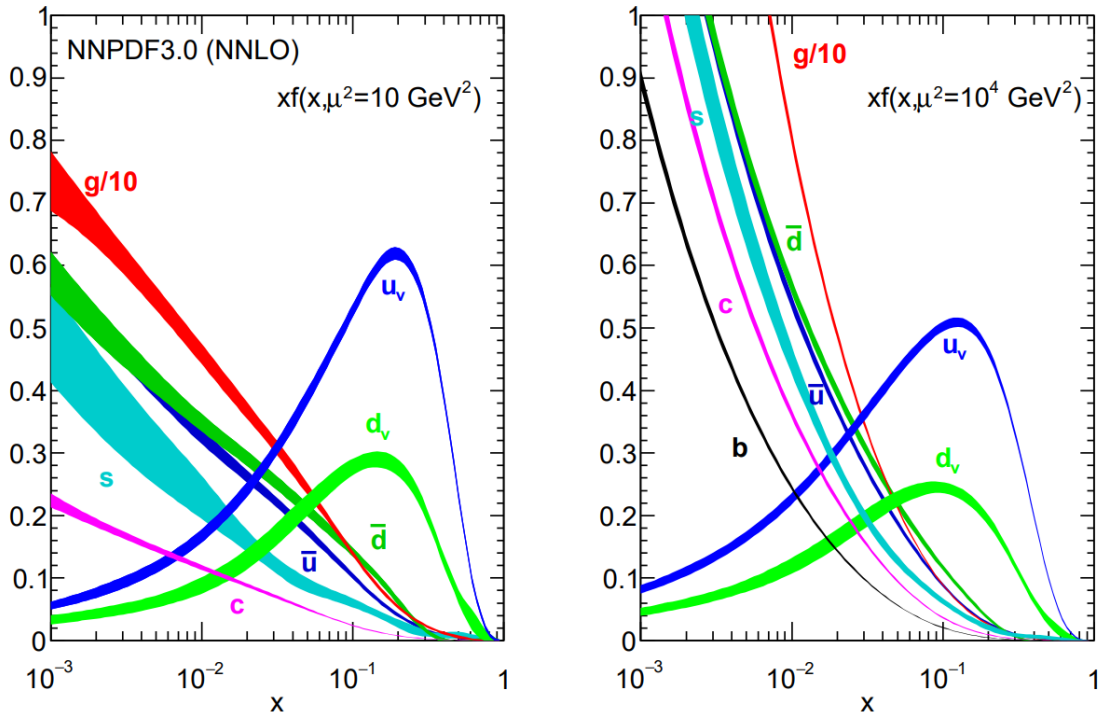

FIGURE 2.2. The bands are the momentum fraction, x, times the unpolarized parton distribution function obtained in NNLO NNPDF3.0 global analysis at scales $\mu^2 = 10$ GeV^2 and $\mu^2 = 100$ GeV^2 [15]

The PDFs and hard scattering processes are included in the calculation of the Matrix Elements (ME) of any interaction. Hard scattering processes can be descibed by Feynman diagrams, a representation of their amplitudes. Combining the PDFs and hard scattering amplitudes gives the probability of a particular interaction occuring. Calculation of the MEs is the first stage of simulation and is done to a specified order in perturbation theory: leading order (LO), next-to-leading order (NLO), etc. Higher order calculations lead to more accurate predictions but grow in complexity exponentially making them harder to calculate both theoretically and computationally, often restricting how accurate a process can be simulated.

2.1.2. Parton Shower Calculation

The next stage of simulating an event is the parton shower. These parton shower calculations deal with the quantum chromodynamic processes. In any interaction the particles that carry color can spontaneously emit gluons which can go on to create more gluons or quark-antiquark pairs. Depending on when this happens in the hard scattering process it is called initial state radiation (ISR) or final state radiation (FSR). The hard scattering partons as well as any additional radiated particles are used as inputs to parton shower calculations which determine how the quarks and gluons proceed through to the final state particles seen in the detector. This includes calculation of hadronization processes and futher decay processes into the final state particles.

2.1.3. Detector Simulation

The final stage of creating an MC event is the detector simulation. The information from the event generators are processed using GEANT4 [16] and a detailed model of the ATLAS detector. GEANT4 simulates how various particles propagate through and interact with the material properties of the detector and where they leave energy which would then be measured by the ATLAS detector in an actual event. The result of this MC event construction flow is a collection of simulated data that is similar in structure to actual data collected using the ATLAS experiment. The energy deposits in both MC and real data are combined using the same software for physics objects are reconstruction. For MC events this allows for comparison between the physics object reconstruction and the truth record, or the types of particles fed into the detector simulation.

2.1.4. Monte Carlo Generators Used for LHC Physics

A variety of different MC generators are used in the creation of simulated events. Different generators specialize in simulating different physics processes to various levels of precision (eg., LO vs. NLO). The MC generators used in this search are summarized in this section.

MadGraph aMC@NLO [17]: An amplitude and event generator at LO and NLO for hard processes. Extendable to various models including effective field theory (EFT) models used in BSM searches. This generator is used to create the signal events searched for in this dissertation: discussed in Section 2.2.

powheg [18, 19]: **Po**sitive **W**eight **H**ardest **E**mission **G**enerator is an NLO event generator that can be interfaced with other generators (i.e. pythia) for showering.

pythia [20]: A generator used most often for QCD final state hard processes and showering. It is commonly interfaced with other generators for showering within the ATLAS detector.

sherpa [21, 22]: A multi-parton LO generator with an emphasis on merging ME and Parton Showering.

A common event file format developed at the Les Houches Accords [23] makes it possible for these generators to be interfaced in a straight forward way, typically with pythia for showering. This allows a specialty generator to be created and used to generate hard processes and then simulate the rest of the event with common showering generators that might lack the ability to simulate the process in question.

2.2. Creation of Flavor Changing Neutral Current Signal Events

To create simulated signal events the typical Standard Model models must be extended to include higher order terms. A Universal FeynRules Output (UFO, [24])

model was created to include dimension 6 operators ([25, 26]). These individual operators are turned on for the specific final state being produced. The original operators can be reduced to a minimal set of coupling to anomalous finals states (i.e. FCNC final states)[27], used for event production. This effective field theory method of signal production is beneficial as it allows for production of signal events that are not dependent on any particular BSM model. This method of including dimension-6 effective operators can be used to produce any of the top FCNC channels, for example in the $t \to qZ$ process [28] and $t \to qH$ [29].

2.2.1. FCNC Events Produced With MadGraph5 aMC@NLO

Signal events have been produced using MadGraph5 aMC@NLO following the Work of Degrande et al.[30]. Before official ATLAS datasets can be produced and the entirety of the event reconstructed through the ATLAS detector, validation of the model must be performed. 10,000 events were produced locally at truth level for each decay channel to compare the kinematics of produced events in $t\bar{t} \to bWq\gamma$ to the kinematics of official production $t\bar{t}$ events.

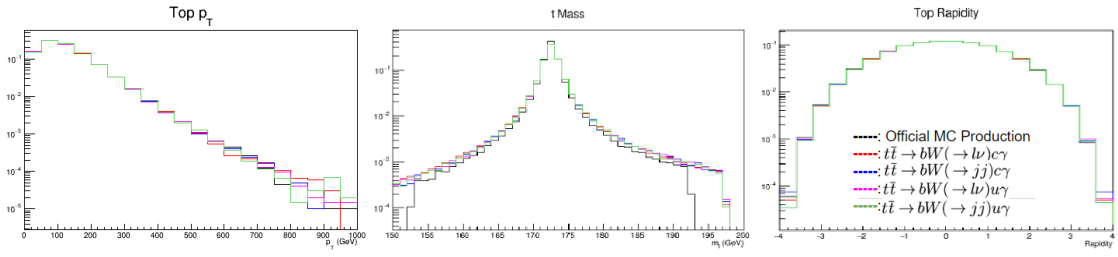

FIGURE 2.3. Normalized kinematics (p_T, m_t, and y_t) of individual top quarks produced by the model for each FCNC final state search and an official $t\bar{t}$ sample.

The minimal couplings mean there is one scalar coupling introduced for each decay mode, $t \to c\gamma$ and $t \to u\gamma$. All possible final states are shown in the figures

in this section: the leptonic and hadronic decays of the W boson from the top quark that decays through the typical standard model decay mode $t \to bW$.

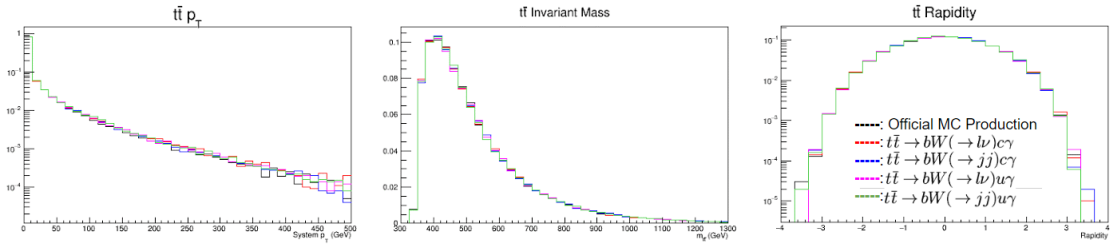

FIGURE 2.4. Normalized kinematics (p_T, $m_{t\bar{t}}$, and $y_{t\bar{t}}$) of the $t\bar{t}$ system produced by the model for each FCNC final state search and an official $t\bar{t}$ sample.

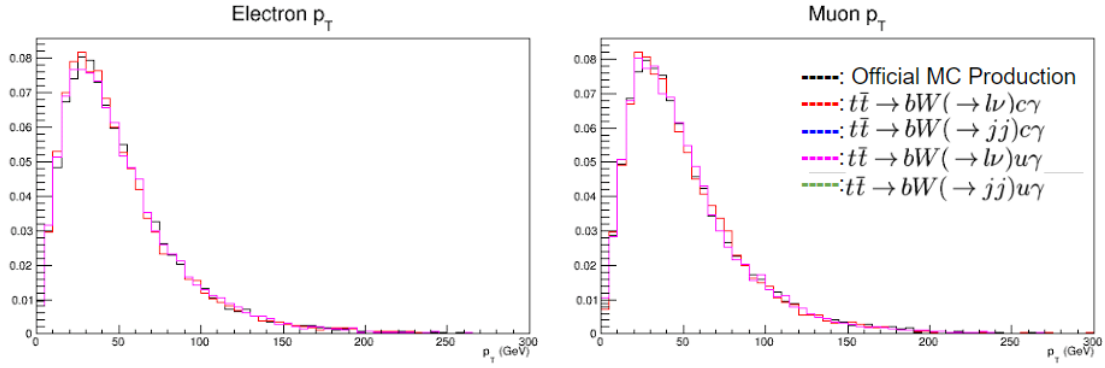

FIGURE 2.5. Normalized p_T of the electron and muons produced by the model for each FCNC final state search and an official $t\bar{t}$ sample.

The lepton validation plots in Figure 2.5 only show events where the W is forced to decay leptonically as well as the official sample which does not have a preference for the final state decay, i.e., the W bosons are allowed to decay leptonically or hadronically. No unexpected deviations from the Standard model produced $t\bar{t}$ samples are seen in any of the validation plots. The deviations seen in Figure 2.6 are misplaced quarks from NLO processes. The shifted mean values in the up and charm p_T spectrum are also expected. In those samples the up or charm quark is coming directly from the top quark as opposed to a W boson, which means it will have significantly boosted momentum.

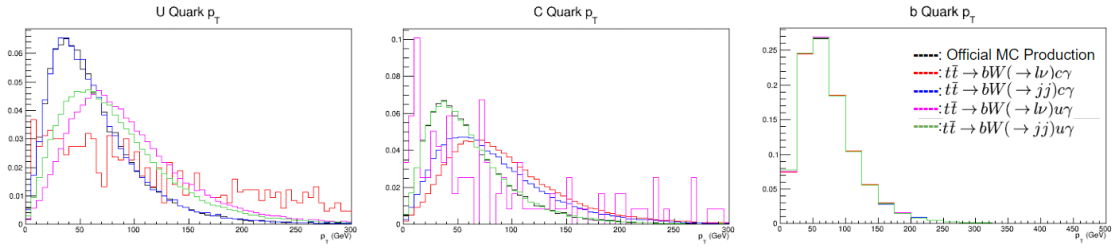

FIGURE 2.6. Normalized p_T of the up, charm, and bottom quarks produced by the model for each FCNC final state search and an official $t\bar{t}$ sample.

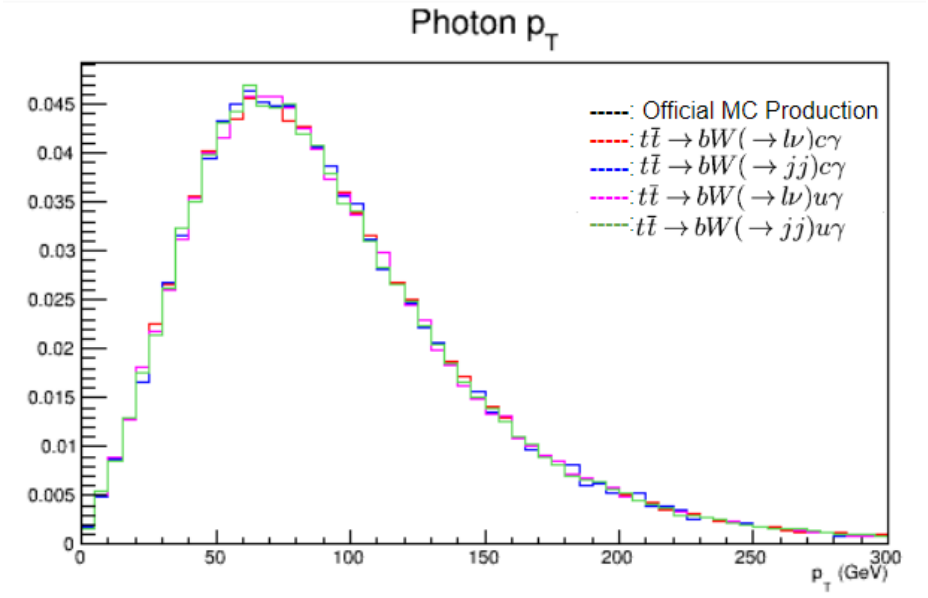

FIGURE 2.7. Normalized p_T of the photons produced by the model for each FCNC final state search and an official $t\bar{t}$ sample, there is 0 contribution from the official $t\bar{t}$ sample.

In the model there are left-and right-handed scalar couplings. Investigation into differences between the kinematics of the quarks produced using each of these couplings is shown in Figure 2.8.

$$\mathcal{L}_{\gamma tc} = -e\bar{c}\frac{i\sigma^{\mu\nu}q_\nu}{m_t}(\lambda^L_{ct}P_L + \lambda^R_{ct}P_R)tA_\mu + h.c.$$

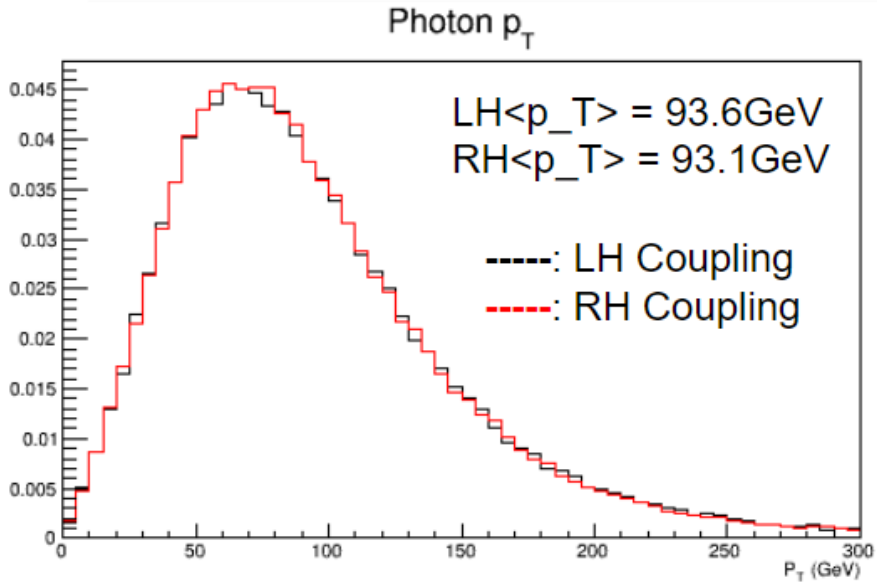

FIGURE 2.8. Normalized p_T of the photons produced by the model using the Left-handed (LH) and Right-handed (RH) couplings

No differences in final state kinematics were shown in the right-handed coupling compared to the left-handed coupling. Due to this, only one coupling value was used in the production. In the end only leptonic decays of the W were produced officially. The leptonic state is simpler to search for than a final state not involving leptons because of the much larger backgrounds from QCD processes. The lepton offers many handles for searching for these rare FCNC decays. Using the leptonic final state it is not necessary to use combinatorics for event reconstruction as each object is unique and comes from one particular object. In this analysis the final state involves a light jet and a photon (from the FCNC decay), and a lepton, photon, and b-jet (from the Standard Model top decay).

2.3. Object Reconstruction

After the events are simulated, or collected in case of real data, the collections of energy deposits within the detector systems must be transformed into meaningful physics objects through reconstruction. Reconstruction is typically done in two major parts using the specialized detectors covered in Chapter I. The Inner Detector and Muon System turn patterns of hits within the tracking detectors into tracks that have direction and momentum information. The calorimeter system transforms the energy deposits within the calorimeters into calibrated energy deposits with a particular position. These tracks and calorimeter deposits are used to create physics objects (electrons, muons, etc.) by using particle identification techniques to reconstruct the underlying physics event. For the analysis presented in this dissertation, the final state signal particles that need to be reconstructed are one lepton (an electron or a muon), one photon, two quarks (one light flavor and one b quark), and one neutrino (missing transverse energy as it is the only particle that does not interact with the detector). Each of these particles has a particular signature in the subdetectors of the ATLAS detector, shown in Figure 2.9.

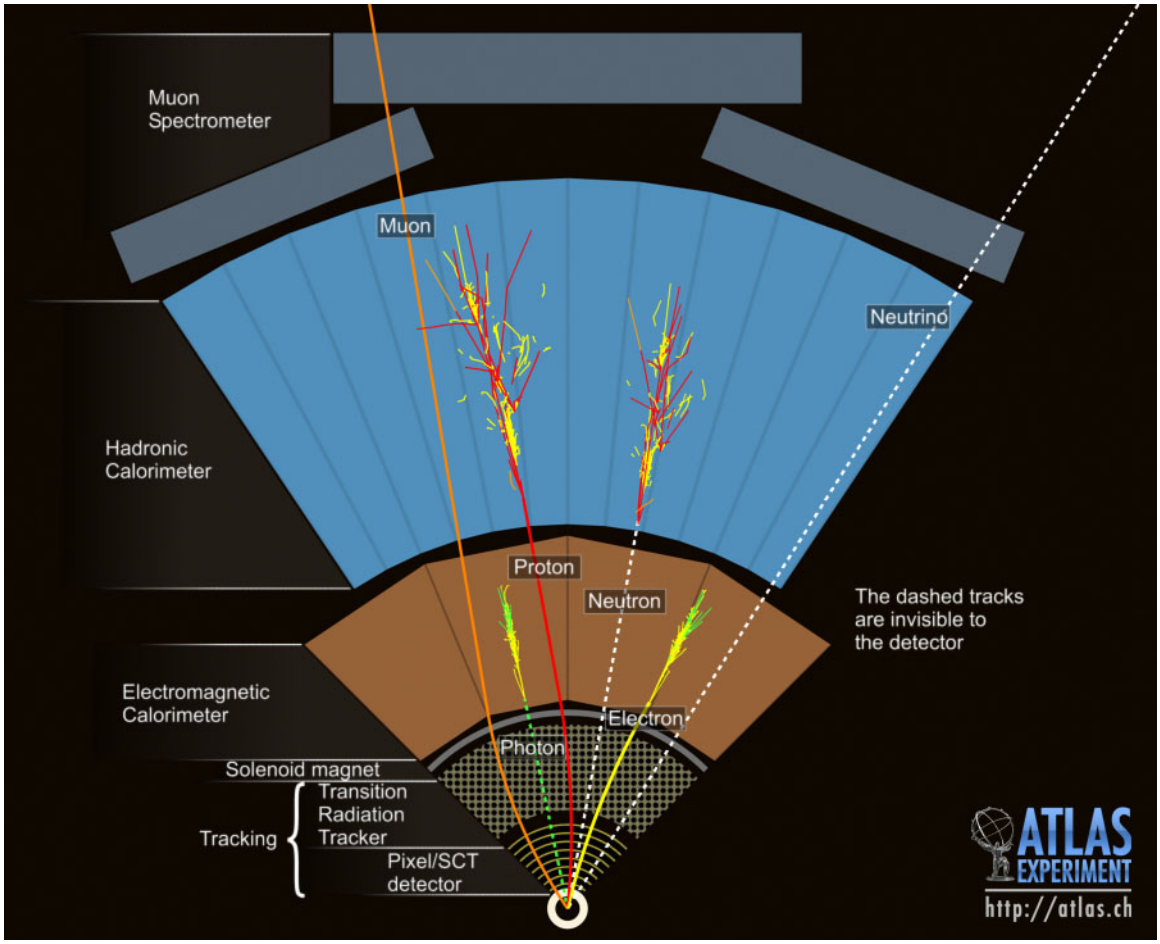

FIGURE 2.9. Cross section of a simulated ATLAS detector showing how various particles interact with ATLAS subsystems. Solid lines indicate interactions while dashed lines indicate that no interactions typically occur in that section of the detector. [31]

2.3.1. Electrons

Electrons interacting with within the ATLAS detector leave a track in the Inner Detector as well as a cluster of energy in the electromagnetic calorimeter. The track and cluster are required to be matched together to be identified as an electron candidate[32]. As electrons move through the detector they create electromagnetic showers through bremsstrahlung which can produce electron-positron pairs. The process continues as the particles continue to give energy to the detector. This

collection of electrons, positrons, and photons creates a signature energy cluster in the calorimeter.

Electron identification algorithms are applied to the electron candidates to separate prompt and isolated electron candidates from electrons that come from backgrounds such as converted photons and misidentified jets. The electron idenification algorithms use a sliding window (3×5 in $\eta \times \phi$) in the high granularity section of the LAr electromagnetic calorimeter to search for electron cluster "seeds" greater than 2.5 GeV. Clusters are created around these seeds to form the electromagnetic shower and remove possible duplicate electron signals by containing them within the cluster. Further pattern recognition for the track fitting allows even larger amounts of energy into the shower to account for bremsstrahlung in the shower shape. Tracks and clusters are then matched to give electron candidates.

Electrons coming from background jets or photon conversion are called non-prompt as they do not originate from a signal object/the primary vertex. In order to reject these electrons, other discriminating variables are used in addition to the track-cluster matching. These variables inclue the amount of energy leakage into the hadronic calorimeter, thee shower development throughout the electromagnetic calorimeter, and the amount of radiation measured in the TRT. Three electron identification working points are used: Loose, Medium, and Tight. Each of these operating points have their own level of background rejection and signal efficiency. Working points with higher background rejection are a subset of those with lower background rejection.

Isolation variables are another useful tool in the identification of signal electrons from converted photons produced in hadron decays and light hadron misidentification. These variables are defined by a cone size around the electron candidate and are the

sum of the transverse variable (momentum or energy) of all of the tracks within the cone, $p_T^{\text{cone0.2}}$ with a cone of $\Delta R = 0.2$ (or 10 GeV/E_T, for high energy electrons) and $E_{T,Topo}^{\text{varcone0.4}}$ with a cone defined in a similar manner.

Because the LAr calorimeter is a sampling calorimeter, the energy deposits must be calibrated and scaled such that the true electron energy is read out and not just the small amount of energy deposited into the active layers as discussed in Section 1.2.4. The energy scale is calibrated to be uniform throughout the detector. Any residual differences between data and simulation are corrected. The calibration strategy was developed for optimal preformance in LHC Run 1[33] and updated for the conditions of LHC Run 2[34].

2.3.2. Muons

Muons behave differently from other particles as they traverse the detector. They act as minimum-ionizing-particles (MIPs) throughout the calorimeter. The Muon Spectrometer (MS), Section 1.2.5, specializes in precision measurements of muons. The Inner Detector (ID) plays a pivotal role in the identification of muons as it offers an independent measure of the muon characteristics. The muron reconstruction process uses a specific set of variables as well[35]. These variables include: *q/p significance*: the difference in the ratio of track charge and momentum measured with the ID and MS, ρ': the difference between the transverse momenta measured with the ID and MS, and χ^2 of the combined track fit using tracks from both the ID and MS.

Muons are separated out into four separate types depending on their interactions with the various subdetectors. The best muon candidates are combined muons that use hits in the MS to trace back to a track in the ID in order to reconstruct the entire

muon track. Segment-tagged muons are muon candidates that leave a track in the ID but only a segment in the MS instead of a full track. Segment-tagged muons can occur because of the muon having low p_T or crossing through a region of the MS with reduced acceptance. Extrapolated muons require only tracks in the MS and are used in regions of η, ϕ phase space that the ID does not cover. Calorimeter-tagged muons are muons identified by MIPs in the calorimeters and are used to find muons that cross the ID and MS in regions where cabling might prevent particle detection.

Muons also have their own set of isolation criteria which is track-based $p_T^{\text{varcone0.3}}$, with a cone of $\Delta\text{R} = \min(0.3, 10 \text{ GeV}/p_T)$. Similar to electrons various working points are available at the analysis level for muons. These working points are named similarly: Loose, Medium, Tight, and High-p_T in order of background rejection.

High p_T jets that punch through the hadronic calorimeter can leave tracks in the MS which could be identified as muons. These would be identified as a bad or a fake muon because of the high-hit multiplicities they leave in the MS as opposed to a single track left by a muon as it is a MIP. Another source of bad muons is a mismeasured ID track that gets incorrectly matched to segments in the MS. Fake muons are a source of fake missing transverse energy, $\not{E}_T$

2.3.3. Photons

Photons behave very similarly to electrons in the calorimeter in that they also produce an electromagnetic shower in the calorimeter. However, they are neutrally charged particles meaning that they should not leave a track in the ID as they do not bend and produce bremsstrahlung photons traveling through the magnetic field. Prompt photons pair-produce electrons in the tracker, but this process can be identified as the associated cluster in the electromagnetic calorimeter

is matched to two tracks with opposite charge. This process produces what is called a converted photon. Unconverted photons have no matching tracks associated with an electromagnetic cluster.

Prompt photons produce narrower energy deposits in the electromagnetic calorimeter and have smaller leakage into the hadronic calorimeter compared to background photons. The energy contained within narrow structure in $\eta \times \phi$ strips compared to the energy containd in a larger section can help identify prompt from non-prompt photons [36]. Cuts on this and the other variables listed in Table 2.1 are tuned to reduce dependency of identification efficiency on the pileup conditions of Run 2.

Category	Description	Name	*loose*	*tight*
Acceptance	$\|\eta\| < 2.37$, with $1.37 \leq \|\eta\| < 1.52$ excluded	-	✓	✓
Hadronic Leakage	Ratio of E_T in the first sampling layer of the hadronic calorimeter to E_T of the EM cluster (used over the range $0.8 < \|\eta\|$ or $\|\eta\| > 1.52$)	R_{had_1}	✓	✓
	Ratio of E_T in the hadronic calorimeter to E_T of the EM cluster (used over the range $0.8 < \|\eta\| < 1.37$)	R_{had}	✓	✓
EM Middle Layer	Ratio of the energy in 3×7 $\eta \times \phi$ cells over the energy in 7×7 cells centered around the photon cluster position	R_η	✓	✓
	Lateral shower width, $\sqrt{(\Sigma E_i \eta_i^2)/(\Sigma E_i) - ((\Sigma E_i \eta_i)/(\Sigma E_i))^2}$, where E_i is the energy and η_i is the pseudorapidity of cell i and the sum is calculated within a window of 3×5 cells	ω_{η_2}	✓	✓
	Ratio of the energy in 3×2 $\eta \times \phi$ strips, over the energy of 3×6 cells centered around the photon cluster position	R_ϕ		✓
EM Strip Layer	Lateral shower width, $\sqrt{(\Sigma E_i (i - i_{\max})^2)/(\Sigma E_i)}$, where i runs over all strips in a window of 3×2 $\eta \times \phi$ strips, and $i_{\max}$ is the index of the highest-energy strip calculated from three strips aroudn the strip with maximum energy deposit	$\omega_{s\ 3}$		✓
	Total lateral shower width $\sqrt{(\Sigma E_i (i - i_{\max})^2)/(\Sigma E_i)}$, where i runs over all strips in a window of 20×2 $\eta \times \phi$ strips, and $i_{\max}$ is the index of the highest-energy strip measured in the strip layer	$\omega_{s\ \text{tot}}$		✓
	Energy outside the core of the three central strips but within seven strips divided by energy within the three central strips	f_{side}		✓
	Difference between the energy associated with the second maximum in the strip layer and the energy reconstructed in the strip with the minimum value found between the first and second maxima	ΔE_s		✓
	Ratio of the enrgy difference between the maximum energy deposit and the energy deposit in the secondary maximum in the cluster to the sum of these energies	E_{ratio}		✓
	Ratio of the energy in the first layer to the total energy of the EM cluster	f_1		✓

TABLE 2.1. Photon identification variables used for *loose* and *tight* photon identification, taken from [36]

2.3.4. Jets

Contrasting with electromagnetic showers produced by electrons and photons, hadronic showers form through QCD processs. Quarks very quickly undergo showering by emitting gluons which further produce quark-antiquark pairs, analogous to the photons and pair-produced electron-positron pairs of electromagnetic showers. When quarks have enough energy they hadronize by producing bound states of particles. These particles are typically pions or mesons that are measured by the ATLAS detector. The top quark is the only quark that decays before hadronization because it decays so fast (5×10^{-25} s). The spray of hadrons coming from a quark from the initial interaction is called a jet and is a collection of detector objects that are traced back and assigned to the quark(s) in the final state of the interaction. These algorithms are called jet-finding algorithms. Pictoral representations of the same event reconstructed with four various algorithms is shown in Figure 2.10.

The jets in this analysis use the anti-k_T algorithm [37] with a radius parameter $R = 0.4$. Jets are not physical objects but collections of clustered particles so how they are defined can change the physics objects that are eventually analyzed. The anti-k_T algorithm is preferred because it is infrared and collinear safe. Infrared safe jet algorithms do not merge two jets with a soft emission between them. Adding or removing a soft term between two jets should not change which objects are called jets. Collinear safe jet algorithms do not change the jet collection if the high transverse momentum particles is split or merged . Another added benefit of the anti-k_T jet finding algorithm is that it produces roughly circular jet objects, thereby simplifying the calculation of the energy density and simplifying the calibration of the jet object.

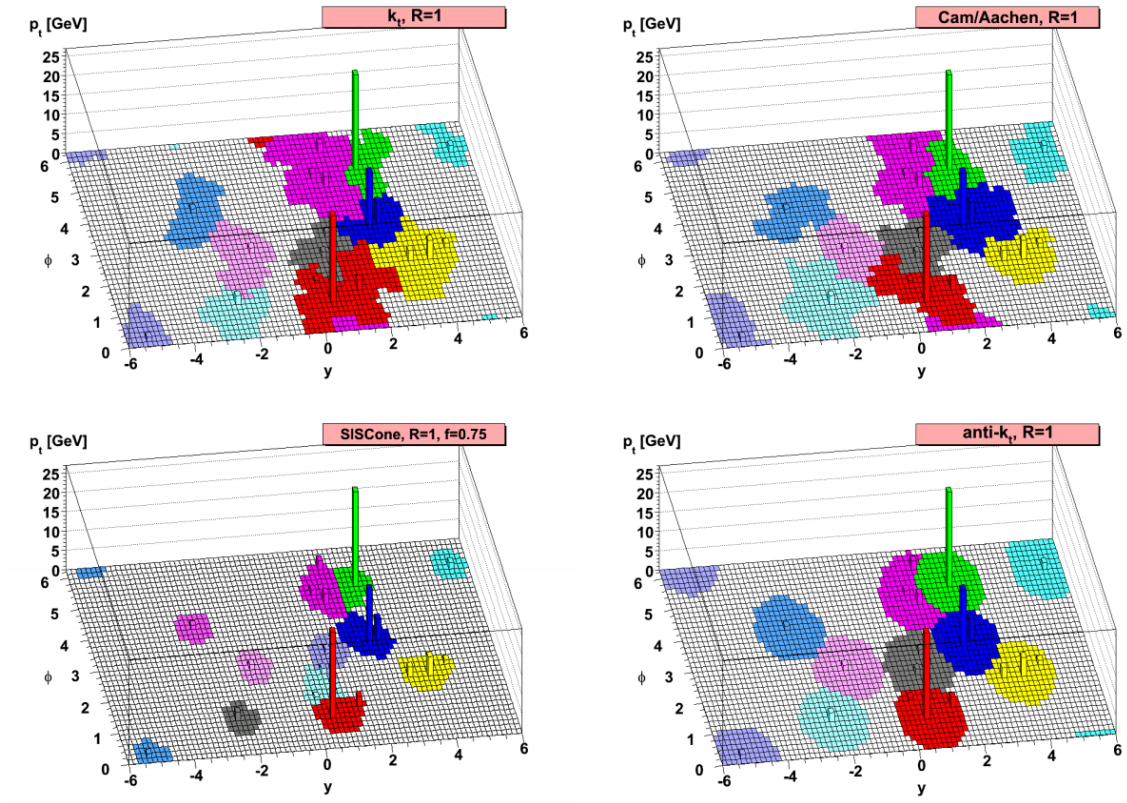

FIGURE 2.10. A sample parton-level event with many random soft jet objects, clustered with four different jets algorithms, illustrating the areas of the resulting hard jets. For kt and Cambridge/Aachen the detailed shapes are in part determined by the specific set of ghosts used, and change when the ghosts are modified [37]

The anti=k_T algorithm calculates the distance between an object i and all possible jet objects j (d_{ij}) and the beam (d_{iB})

$$d_{ij} = \min(k_{ti}^{2p}, k_{tj}^{2p})\frac{\Delta_{ij}^2}{R}, \qquad d_{iB} = k_{ti}^{2p}$$

where k_{ti} is the transverse momentum, Δ is the distance between the objects, and $p = -1$. This is a general form for the type of algorithm where the inclusive k_T algorithm has a p value of 1 and the inclusive Cambridge/Aachen algorithm has a p value of 0 [38]. The algorithm then follows that if d_{ij} is smaller than d_{iB} then objects

i and j are merged, otherwise i is labeled as a jet and removed from the list of entries of possible jet objects. This is repeated for all entries in the list of possible jet objects.

Jet cleaning is also applied to remove events with jets built from known noisy parts of the calorimeter due to particular calorimeter cells or non-collision background in those areas [39]. To reduce selecting jets that originate from pileup interactions, another requirement on the jet object is made on the jet vertex tagger [40, 41] as follows:

1. For jets with 20GeV $< p_T <$ 60GeV and $|\eta| < 2.4$: if any jet is bad AND that jet is not marked as pileup by JVT, then reject the event

2. For jets with 20GeV $< p_T <$ 60GeV and $|\eta| \geq 2.4$: if any jet is bad, then reject the event

3. For jets with $p_T \geq$ 60GeV: if any jet is bad, then reject the event

2.3.4.1. B-Jets

While jets originate from any quark, jets coming from b quarks can be identified due to their decay products. B quarks hadronize into b-hadrons which have a relatively long lifetime compared to many other hadrons produced from light quarks. The longer lifetime and the relativistic speeds at which the hadrons travel mean the particle travels a measureable distance before it decays $(400 - 500\mu m)$[42]. Thus, the vertex reconstructed from the energy coming from a b hadron decay can be traced back to a point that does not correspond to the primary vertex of the event. A pictoral representation of a b quark decay is shown in Figure 2.11. The b-jet vertex is called the secondary vertex.

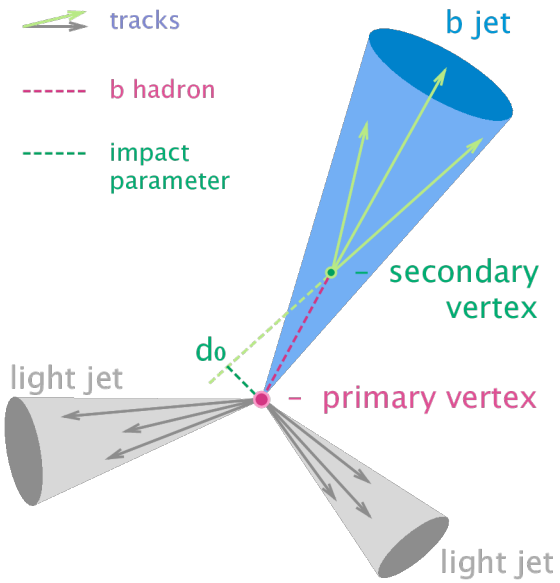

FIGURE 2.11. Pictoral representation of an event with a b-jet showing the secondary vertex and impact parameter [43]

In addition to the secondary vertex, other variables are helpful in identifiying jets coming from b quarks. By back tracing the tracks within the displaced vertex the minimum distance between the track and the interaction point can be measured, known as the impact parameter. Reconstructing the decay chain of the jet is also used in determining the providence of the jet. This information is used in a multivariate analysis (MVA) to identify jets coming from b quarks and reject jets coming from light quarks.

The MVA used in this analysis is the MV2c10, the discriminant used for b-jet identification [44]. The output distributions for various flavors of jets as well as background rejection and signal efficiency plots are shown in Figure 2.12. The c10 in the algorithm name refers to the background training sample of the MVA consisting of a 10% fraction of c-jets. The 77% efficiency fixed-cut working point for b-jet identification was chosen for this analysis, discussed in Section **??**. Differences in efficiency of b-tagging between data and simulation is taken into account with working

point specific scale factors provided by the ATLAS Flavour Tagging Combined Performance group.

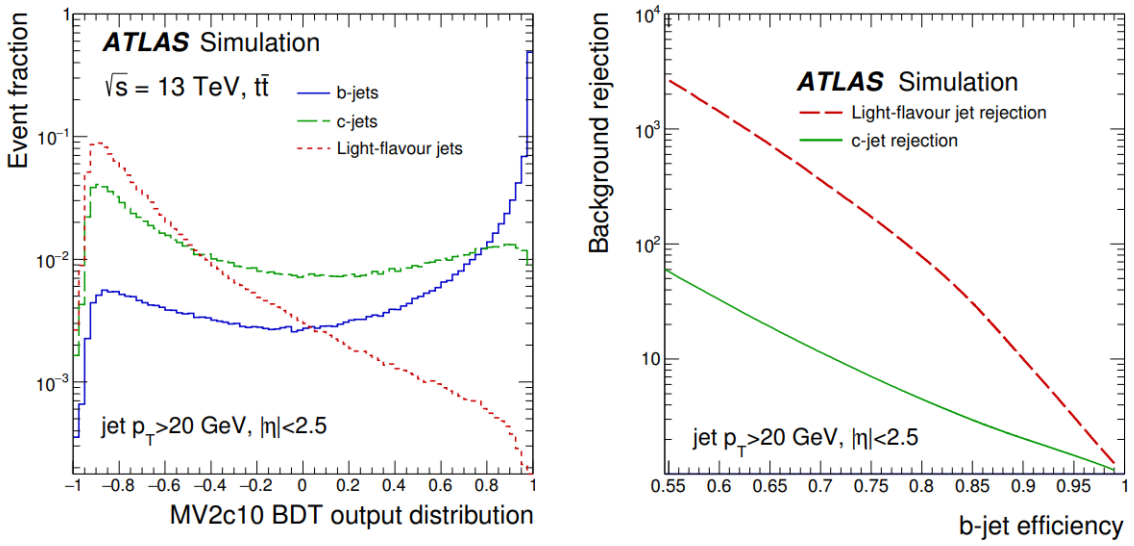

(a) (b)

FIGURE 2.12. The MV2c10 output for b, c, and light flavored jets in simulated $t\bar{t}$ and the background rejection as a function of the b-jet efficiency [45]

2.3.5. Missing Transverse Energy

The remaining signal object that has yet to be discussed is the neutrino coming from the W boson decay. Neutrinos do not interact with the detectors as they pass through the ATLAS detector. The only way to measure any properties of the neutrino in ATLAS events is to use conservation of momentum. As previously mentioned the collision energy is unknown as partons do not carry a consistent fraction of the beam proton energy. However, in the transverse plane to the beamline the total momentum is known to be very small. Before the collision there is on the order of 1 GeV of momentum in the transverse plane. Therefore, the total transverse momentum of the collision products should be approximately zero.

Any imbalance in the momentum is referred to as Missing Transverse Momentum ($\not\!\!E_T$). The negative vector sum of all reconstructed objects plus an additional soft term are used to calculate the missing energy in the x-plane and the y-plane[46]. A magnitude and an aziumuthal angle are calculated to give the $\not\!\!E_T$ vector in the transverse plane but this does not directly correspond to a neutrino which also has a momentum in the z direction.

2.3.5.1. Neutrino Reconstruction

In this analysis the signal contains only one source of missing energy, therefore all of the missing energy can be used to reconstruct a neturino object. There is an ambiguity in the choice of the neutrino z-momentum. To find the z-momentum a χ^2 minimization is done:

$$\chi^2 = \chi^2_{\mathrm{SMTop}} + \chi^2_{\mathrm{W}}$$

$$\chi^2 = \frac{(m_{\mathrm{bjet},l,\nu} - m_t)^2}{\sigma^2_{\mathrm{SMTop}}} + \frac{(m_{l,\nu} - m_W)^2}{\sigma^2_W}$$

The widths $sigma_{\mathrm{SMTop}}$ and σ^2_W are determined from signal Monte Carlo. The event objects are combined to calculate the invariant mass of the top quark (the combination of the b-jet, lepton, and neutrino) and the W boson (combination of the lepton and neutrino). The χ^2 minimization is is done while varying the z-momentum of the neturino. The neutrino momentum that corresponds to the smallest χ^2 value is given assigned to the neutrino object for further use in the analysis. The χ^2 values are also used as a discriminating variable and fed into a neural network (Section **??**).

REFERENCES CITED

[1] Fabian Kuger. Signal formation processes in micromegas detectors and quality control for large size detector construction for the atlas new small wheel. 08 2017.

[2] Esma Mobs. The CERN accelerator complex. Complexe des accélérateurs du CERN. Jul 2016. General Photo.

[3] The ATLAS Collaboration. Luminosity public results run 2, 2019.

[4] The ATLAS Experiment at the CERN Large Hadron Collider. *J. Instrum.*, 3:S08003. 437 p, 2008.

[5] M Capeans, G Darbo, K Einsweiller, M Elsing, T Flick, M Garcia-Sciveres, C Gemme, H Pernegger, O Rohne, and R Vuillermet. ATLAS Insertable B-Layer Technical Design Report. Technical Report CERN-LHCC-2010-013. ATLAS-TDR-19, Sep 2010.

[6] *ATLAS inner detector: Technical Design Report, 1.* Technical Design Report ATLAS. CERN, Geneva, 1997.

[7] Yosuke Takubo. ATLAS IBL operational experience. *PoS*, Vertex2016:004, 2017.

[8] Karolos Potamianos. The upgraded Pixel detector and the commissioning of the Inner Detector tracking of the ATLAS experiment for Run-2 at the Large Hadron Collider. *PoS*, EPS-HEP2015:261, 2015.

[9] Bartosz Mindur. ATLAS Transition Radiation Tracker (TRT): Straw tubes for tracking and particle identification at the Large Hadron Collider. *Nucl. Instrum. Meth.*, A845:257–261, 2017.

[10] *ATLAS liquid-argon calorimeter: Technical Design Report.* Technical Design Report ATLAS. CERN, Geneva, 1996.

[11] *ATLAS tile calorimeter: Technical Design Report.* Technical Design Report ATLAS. CERN, Geneva, 1996.

[12] ATLAS Outreach. ATLAS Fact Sheet : To raise awareness of the ATLAS detector and collaboration on the LHC. 2010.

[13] Moritz Backes. The ATLAS Trigger System: Ready for Run-2. *PoS*, LeptonPhoton2015:045, 2016.

[14] Chaowaroj Wanotayaroj and Jim Brau. Search for a Scalar Partner of the Top Quark in the Jets+MET Final State with the ATLAS detector, Nov 2016. Presented 25 Oct 2016.

[15] M. Tanabashi et al. Review of Particle Physics. *Phys. Rev.*, D98(3):030001, 2018.

[16] S. Agostinelli et al. GEANT4: A Simulation toolkit. *Nucl. Instrum. Meth.*, A506:250–303, 2003.

[17] J. Alwall, R. Frederix, S. Frixione, V. Hirschi, F. Maltoni, O. Mattelaer, H. S. Shao, T. Stelzer, P. Torrielli, and M. Zaro. The automated computation of tree-level and next-to-leading order differential cross sections, and their matching to parton shower simulations. *JHEP*, 07:079, 2014.

[18] Stefano Frixione, Paolo Nason, and Carlo Oleari. Matching NLO QCD computations with Parton Shower simulations: the POWHEG method. *JHEP*, 11:070, 2007.

[19] Simone Alioli, Paolo Nason, Carlo Oleari, and Emanuele Re. A general framework for implementing NLO calculations in shower Monte Carlo programs: the POWHEG BOX. *JHEP*, 06:043, 2010.

[20] Torbjorn Sjostrand, Stephen Mrenna, and Peter Z. Skands. A Brief Introduction to PYTHIA 8.1. *Comput. Phys. Commun.*, 178:852–867, 2008.

[21] T. Gleisberg, Stefan. Hoeche, F. Krauss, M. Schonherr, S. Schumann, F. Siegert, and J. Winter. Event generation with SHERPA 1.1. *JHEP*, 02:007, 2009.

[22] Enrico Bothmann et al. Event Generation with Sherpa 2.2. *SciPost Phys.*, 7:034, 2019.

[23] Johan Alwall et al. A Standard format for Les Houches event files. *Comput. Phys. Commun.*, 176:300–304, 2007.

[24] Celine Degrande, Claude Duhr, Benjamin Fuks, David Grellscheid, Olivier Mattelaer, and Thomas Reiter. UFO - The Universal FeynRules Output. *Comput. Phys. Commun.*, 183:1201–1214, 2012.

[25] R. A. Coimbra, P. M. Ferreira, R. B. Guedes, O. Oliveira, A. Onofre, R. Santos, and Miguel Won. Dimension six FCNC operators and top production at the LHC. *Phys. Rev.*, D79:014006, 2009.

[26] B. Grzadkowski, M. Iskrzynski, M. Misiak, and J. Rosiek. Dimension-Six Terms in the Standard Model Lagrangian. *JHEP*, 10:085, 2010.

[27] J. A. Aguilar-Saavedra. A Minimal set of top anomalous couplings. *Nucl. Phys.*, B812:181–204, 2009.

[28] Zenro Hioki, Kazumasa Ohkuma, and Akira Uejima. Effective Lagrangian Approach to Top Decay via Flavor Changing Neutral Current. In *29th International Conference on Lepton and Photon Interactions (LP2019) Toronto, Ontario, Canada, August 5-10, 2019*, 2019.

[29] Artur Amorim, Juan Pedro Araque, Nuno Filipe Castro, Jose Santiago, and Rui Santos. Production of tγ, tZ and tH via Flavour Changing Neutral Currents. *PoS*, TOP2015:067, 2016.

[30] Celine Degrande, Fabio Maltoni, Jian Wang, and Cen Zhang. Automatic computations at next-to-leading order in QCD for top-quark flavor-changing neutral processes. *Phys. Rev.*, D91:034024, 2015.

[31] Joao Pequenao. Event Cross Section in a computer generated image of the ATLAS detector. Mar 2008.

[32] Morad Aaboud et al. Electron reconstruction and identification in the ATLAS experiment using the 2015 and 2016 LHC proton-proton collision data at $\sqrt{s} =$ 13 TeV. *Eur. Phys. J.*, C79(8):639, 2019.

[33] Electron and photon energy calibration with the ATLAS detector using LHC Run 1 data. *Eur. Phys. J.*, C74(10):3071, 2014.

[34] ATLAS Collaboration. Electron and photon energy calibration with the ATLAS detector using data collected in 2015 at $\sqrt{s} = 13$ TeV, Aug 2016.

[35] Sébastien Rettie. Muon identification and performance in the ATLAS experiment. *PoS*, DIS2018:097, 2018.

[36] Morad Aaboud et al. Measurement of the photon identification efficiencies with the ATLAS detector using LHC Run 2 data collected in 2015 and 2016. *Eur. Phys. J.*, C79(3):205, 2019.

[37] Matteo Cacciari, Gavin P. Salam, and Gregory Soyez. The anti-k_t jet clustering algorithm. *JHEP*, 04:063, 2008.

[38] M. Wobisch and T. Wengler. Hadronization corrections to jet cross-sections in deep inelastic scattering. In *Monte Carlo generators for HERA physics. Proceedings, Workshop, Hamburg, Germany, 1998-1999*, pages 270–279, 1998.

[39] Selection of jets produced in 13TeV proton-proton collisions with the ATLAS detector. Technical Report ATLAS-CONF-2015-029, CERN, Geneva, Jul 2015.

[40] The ATLAS collaboration. Tagging and suppression of pileup jets. 2014.

[41] S. Schramm. Howtocleanjets2016 : Jet-based event cleaning, 2016.

[42] Albert M Sirunyan et al. Measurement of b hadron lifetimes in pp collisions at $\sqrt{s} = 8$ TeV. *Eur. Phys. J.*, C78(6):457, 2018. [Erratum: Eur. Phys. J.C78,no.7,561(2018)].

[43] N. Bartosik. File:b-tagging diagram.png, 2016.

[44] Francesco Armando Di Bello. Optimisation of the ATLAS b-tagging algorithms for the 2017-2018 LHC data-taking. *PoS*, EPS-HEP2017:733, 2017.

[45] Morad Aaboud et al. Measurements of b-jet tagging efficiency with the ATLAS detector using $t\bar{t}$ events at $\sqrt{s} = 13$ TeV. *JHEP*, 08:089, 2018.

[46] Morad Aaboud et al. Performance of missing transverse momentum reconstruction with the ATLAS detector using proton-proton collisions at $\sqrt{s} =$ 13 TeV. *Eur. Phys. J.*, C78(11):903, 2018.